Kirk-Othmer Encyclopedia of Chemical Technology.
Copyright © John Wiley & Sons, Inc. All rights reserved.

PHOTODETECTORS

1. Photodetectors

Photons impinging upon matter interact in a manner determined by the nature of the chemical bonds in the material and the energy of the incident photons. Interacting photons may be reflected, refracted, diffracted, transmitted, or absorbed. Each of these phenomena can be used to measure some parameter of interest in chemical analysis. Photoassisted chemical analytical techniques require an accurate, sensitive method of photon detection and quantification. Photographic film proved to be the first useful method for such evaluations. Later, photomultiplier tubes provided the means to improve many photoanalytical techniques. With the advent of semiconductor technology, numerous single-element, broad-spectrum photodetecting devices were developed and applied to the task. Most recently, photodetector technology has entered the age of high density integration. Large-area photon detectors are becoming commonplace in most analytical equipment. The advances afforded by these devices have allowed for significant improvements in the performance of systems designed for photo-analytical chemical analysis in general, and specifically for spectroscopic-based equipment. A working knowledge of the operation and limitations of photodetectors is therefore necessary for the modern chemist.

Photodetector devices convert electromagnetic radiation or photons to electric signals that can be processed to obtain the spectral, spatial, and temporal information inherent in the radiation. Photodetectors, as indicated in Table 1, may be operated in many modes. The more popular ones are photoconductors, photodiodes, charge-transfer devices, and the pyroelectrics. The detectors may be used as single elements such as in street light controls, film camera exposure control, or motion detectors for security. Photodetectors also find application in the form of linear arrays used in analytical spectrometers, night-vision equipment, in small, low cost spectrometers for the control of building ventilation and environmental pollution monitoring, or configured as large matrix arrays found in video cameras.

2. Principles

2.1. Photon-Absorption and Thermal Emission

The basic detection process, as shown in Figure 1, is the generation of free electrons, holes, or both by the absorption of photon energy (1–4). The absorption may be intrinsic, ie, creating a free electron–hole pair, or extrinsic, creating a free hole or electron. The process can be indirect whereby the absorbed photon energy raises the lattice temperature (thermal detection) and a phonon generates the free charged particle. The change in free charge is sensed in an amplifier circuit as a signal voltage or current. Random generation of free charge is the source of detector noise. The detector geometry, spectral response, electrical bias, and temperature are adjusted to optimize the signal-to-noise ratio. The absorption efficiency (photon-to-electron conversion) is a critical issue. The detector surface is typically coated to minimize reflections at a particular wavelength and

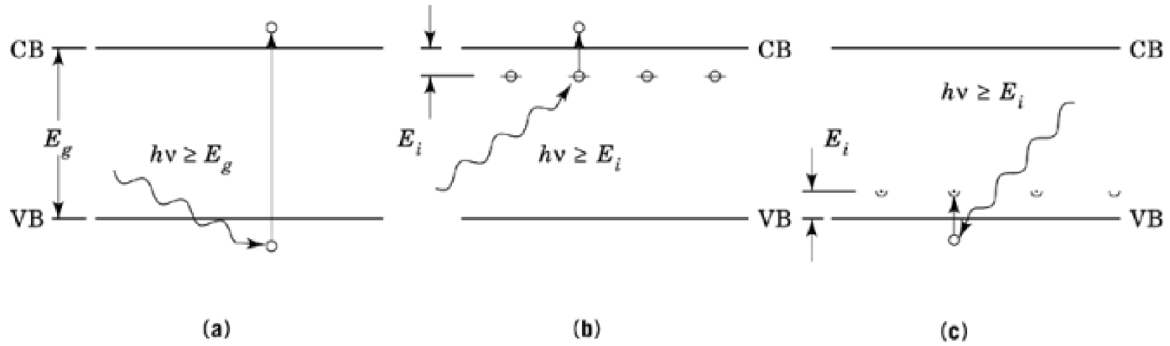

Fig. 1. Photoexcitation modes in a semiconductor having band gap energy, E_g, and impurity states, E_i. The photon energy $h\nu$ must be sufficient to release an electron (◦) into the conduction band (CB) or a hole (⁎) into the valence band (VB): (**a**) an intrinsic detector; (**b**) and (**c**) extrinsic donor and acceptor devices, respectively.

the internal efficiency is given by $1 - \exp(-\alpha x)$. Because the absorption coefficient α is typically 3000 cm^{-1} for intrinsic detection and 3 cm^{-1} for the extrinsic case, detector thickness, x, has a large range of values.

Table 1. Semiconductor Photodetectors in General Use

Bandwidth, μm	Mode[a,b]	Temp., K	Material	Pixel size, μm	Focal plane size	Principal use	Cutoff wave-length, μm	Response time, μs	Responsivity, V/W	$D*$, cm·Hz$^{1/2}$/W
					Ultraviolet					
0.200–0.400	CCD	300	Si	10–30	2000×4000	Astronomy	1.1		1×10^{11}	5×10^{13}
0.400–0.700[c]	CCD	300	Si	10–30	488×640–2000×2000	Video Camera	1.1		2×10^{10}	5×10^{13}
	PC	300	CdS	100–1000	<100	Light meter	0.7	100,000	1×10^{6}	1×10^{13}
	PV	300	Si	30–200	few	Optical switch	1.0	0.01–10	0.5[d]	5×10^{13}
	PV	300	GaAsP	30–200	few	Optical switch	0.8	0.1–10	0.2[d]	1×10^{13}
					Short Wavelength Infrared					
1–3	PV	240	InGaAs	25–200	1×512	Spectroscopy	2.5	1	0.2[d]	2×10^{12}
	PV	200–300	InGaAs	25–200	512×512	Imaging	1.7	1	0.2[d]	2×10^{12}
	PV	200–300	HgCdTe	40–400	256×256–1000×1000	Astronomy; mapping	2.9	10	2.0[d]	2×10^{12}
	PC	200–300	PbS	40–400	10×3000	Mapping	3.3–2.7	1000–300	5×10^{4}–1×10^{3}	5×10^{11}–1×10^{11}
					Mid-Wavelength Infrared					
3–5	PC	150–220	HgCdTe	40–60	1×100	Night scope; heat sensing	5.0	10	1×10^{5}	1×10^{11}
	PC	77–200	PbSe	50–80	1×100	Heat sensing	5.8[e]	150[e]	1×10^{6}[e]	2×10^{10}[e]
	PC[f]	60–90	Ge:Au	80–200	Few	Fast response	7.8	0.1	1×10^{4}	1×10^{10}
	PV	60–90	InSb	40–60	512×512	Thermal imaging	5.25	1	3.4[d]	1×10^{11}
	PV	120	HdCdTe	40–60	512×512	Thermal imaging	5.0	5	3.4[d]	1×10^{11}
	SB[g]	60–80	Si:Pt	40–60	480×640	Thermal imaging	4.6	1	0.03[d]	3×10^{9}
					Long Wavelength Infrared					

Table 1. *Continued*

Bandwidth, μm	Mode[a,b]	Temp., K	Material	Pixel size, μm	Focal plane size	Principal use	Cutoff wavelength, μm	Response time, μs	Responsivity, V/W	$D*$, cm·Hz$^{1/2}$/W
8–12	PC	70–100	HgCdTe	40–60	1 × 512	Thermal imaging	12.2	1	1×10^5	3×10^{10}
	PV	60–90	HgCdTe	40–60	512 × 512	Thermal imaging	10.5	1	6.5[d]	5×10^{10}
	QWIP[h]	50–77	GaAs/AlGaAs	40–60	486 × 640	Thermal imaging	9.4[i]	1[i]	0.2d,[i]	1×10^{10}[i]
5–150	PC[f]	30–40	Ge:Hg	50–200	1 × 200	Thermal imaging	13	0.1	5×10^5	3×10^{10}
	PC[f]	20–30	Ge:Cd	50–200	1 × 100	Spectrometry	28[j]	1[j]	5×10^5[j]	3×10^{10}[j]
	PC[f]	5–15	Ge:Zn	50–200	1 × 100	Spectrometry	37[k]	1[k]	5×10^5[k]	2×10^{10}[k]
	PC[f]	4–10	Si:Ga	50–100	64 × 256	Threat detection	18	1	5×10^5	2×10^{10}
	PC[f]	4–10	Si:As	50–100	64 × 256	Threat detection	22	1	5×10^5	2×10^{10}
					Broadband					
0.200–200	Bol[l]	300	α-silicon	40–60	240 × 320	Thermal imaging	Full band	10,000	1×10^6	5×10^8
	Bol[l]	300	VO	40–60	640 × 480	Thermal imaging	Full band	10,000	1×10^6	5×10^8

[a] Bol = bolometer; CCD = charge – coupled device; PC = photoconductor; PV = photovoltaic; QWIP = quantum well infrared photodetector; and SB = Schottky barrier.
[b] Detectors are all intrinsic unless otherwise noted. See Fig. 1.
[c] Visible bandwidth; $\text{near in} = 0.700 - 1.00\ \mu\text{m}$.
[d] Units are A/W.
[e] Values are for a temperature of 190 K.
[f] Detector is extrinsic.
[g] Detector is an internal photoemission (IPE) device.
[h] Detector is a superlattice (SL) device.
[i] Values are for a temperature of 77 K.
[j] Values are for a temperature of 15 K.
[k] Values are for a temperature of 6 K.
[l] Detector is a thermal device.

There are important figures of merit (5) that describe the performance of a photodetector. These are, responsivity, noise, noise equivalent power, detectivity, and response time (2, 6). However, there are several related parameters of measurement, eg, temperature of operation, bias power, spectral response, background photon flux, noise spectra, impedance, and linearity. Operational concerns include detector–element size, uniformity of response, array density, reliability, cooling time, radiation tolerance, vibration and shock resistance, shelf life, availability of arrays, and cost.

Photodetectors exhibit well-defined, cutoff wavelength thresholds, the positions of which are determined by the magnitudes of the band gap activation energy, E_g, or impurity-activation energy, E_i. The cutoff wavelength, λ_c, corresponds to a photochemical activation energy, E, where,

$$\lambda_c = \frac{hc}{E} \qquad (1)$$

The product of Planck's constant and the velocity of light, $hc = 1.24$ when E is expressed in eV and λ_c in μm. Because the absorption coefficient typically is a weak function of wavelength above the threshold energy, the spectral response approximates that of the ideal quantum counter. The interest in semiconductor photodetectors

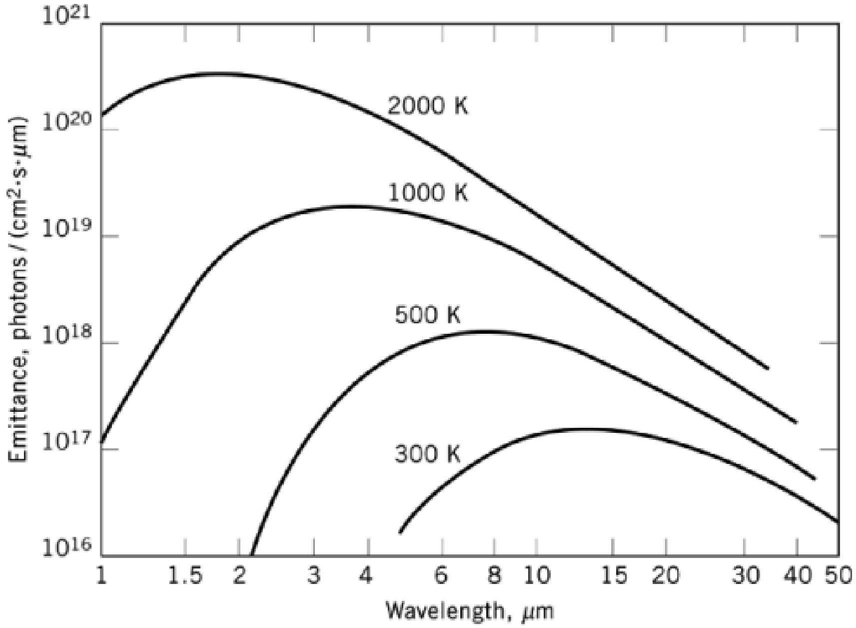

Fig. 2. Blackbody radiated photon flux interval distribution from ambient temperature up to 2000 K. Ambient objects do not have detectable flux for detectors of cutoff wavelengths $<$ ca 3 μm.

with cutoff wavelengths longer than 3 μm results from their extreme sensitivity to variations in photon flux emitted from gray-body objects that are characterized by time and spatial variations in temperature and emissivity. Although some applications require detection of narrow-band radiation, eg, atomic emission spectra and radiation from hot gases, most uses of infrared (ir) detectors involve detection of variations in photon flux from objects near ambient temperature. Typically, a lens system images the scene of interest on a single detector element, a linear array of detector elements, or an area array (7, 8). The ir detector is exposed to the signal photon flux through the optics. The ambient background photon flux, φ_B, is often much greater than the signal flux and determines the ultimate system performance. The background portion, φ_B, in photons/(cm^2·s) may be calculated from Planck's radiation law.

2.2. Blackbody Emittance

Representative blackbody emittance (9, 10), calculated as a power spectral density, is shown in Figure 2. The wavelength, λ, of peak power density for a blackbody at temperature T, is given by Wien's displacement law:

$$\lambda_m T = 2898\ \mu\mathrm{m\,K} \qquad (2)$$

where λ_m is the wavelength of maximum power density and T is temperature in K. The peak spectral power density or emittance, in W/(cm^2·μm), is given by

$$M(T)_m = 1.288 \times 10^{-15}\, T^5\, \mathrm{W}/\left(\mathrm{cm}^2 - \mu\mathrm{m}\right) \qquad (3)$$

for each square centimeter of emitting surface and μm wavelength at the peak value. The total power density, W, as integrated over all wavelengths in W/cm^2, is given by the Stefan–Boltzmann law:

$$W = 5.67 \times 10^{-12}\, T^4\, \mathrm{W/cm^2} \qquad (4)$$

which expresses the total rate of emission in a 2π steradian solid angle from an element area on a blackbody surface. The very strong dependence of W on temperature and the sharp decline of emittance for wavelengths somewhat less than the peak wavelength results in very low ambient background flux density for ambient temperatures $<$ 320 K and detectors having cutoff wavelengths $<$3 μm. Short wavelength detectors such as silicon charge-coupled devices (CCDs) do not work in the ir for this reason but are excellent when hot sources are available such as light bulbs (1500 K) and the sun (6000 K). It is apparent from Figure 2 that detection of ambient temperature objects (night vision) requires a detector having cutoff wavelength $>$4 μm. Detectors having response beyond 8 μm generally are better for thermal imaging applications. However, system sensitivity is dependent also on several other factors: detector quantum efficiency, detector noise, electronics noise, number of detectors on the focal plane (ie, noise bandwidth), sampling rate, width of spectral band, optical aperture, and detector element size.

3. Figures of Merit

3.1. Responsivity

A detector responds to variations in photon-flux density φ_s by producing a signal voltage, V_s, or current. The background photon flux, φ_B, may result in an offset voltage that can be nulled by a differentiating circuit, because φ_B is constant for a given measurement. For most detectors, the output voltage depends on the additive effect of φ_s over the detector area, A. Each photon has energy $h\nu$. The integrated power density over a spectral interval is J_s. The ratio of signal voltage (amperes or electrons) to the signal photon rate is the responsivity, R_V, in units of V/W.

$$R_V = \frac{V_s}{AJ_s} \qquad \mathrm{V/W} \qquad (5)$$

V_s usually is linear with J_s for low intensity, but saturates at the higher signal-flux levels where the photon flux disrupts the thermal equilibrium of the semiconductor electronic states. When J_s refers only to those photons capable of generating free carriers, R_V is considered the spectral responsivity, R_λ. When the flux includes all wavelengths, R_V is called the blackbody responsivity, R_bb. The responsivity of photodiodes is often expressed in amperes per watt (A/W) because the diode is utilized as a current generator when connected to an integrating amplifier. The ideal responsivity for a photodiode is given by $\eta q / E_\mathrm{g}$ where η is the quantum efficiency, q is the charge of an electron, and E_g is the band gap energy. Most commercial detectors achieve $>$ 50% of the ideal responsivity except for the silicide detectors that typically show $<$ 2% of the ideal responsivity.

3.2. Noise

Performance of a system, whether it be an analytical spectrometer or thermal imager, improves as the detector noise is lowered until amplifier noise becomes the dominant noise source, provided that the responsivity is not reduced faster than the detector noise. A well-engineered approach to improvement of system sensitivity consists of (1) lowering amplifier noise consistent with system bandwidth, power, weight, size, and cost budgets; (2) perfecting the detector material and fabrication processes for least defects to achieve lowest noise; and (3) designing the detector mode of operation, geometry, response time, and bias power for highest responsivity.

The operating parameters of the detector are often adjusted to increase responsivity and noise to the point where the detector noise just exceeds the amplifier noise if in fact that is possible.

Although photodetector noise (11) originates as random fluctuations of photons or electrical carriers, it is measured using the Fourier transform process into a frequency function for purposes of analysis. The noise spectrum is characterized by frequency dependent noise at low frequency (called l/f noise), generation recombination (g-r) noise in a midrange, and system noise at high frequency. At low frequency, noise typically varies inversely as the square root of frequency and is a result of surface traps and/or fluctuating defects (12, 13). This noise is often reduced by surface passivation to reduce the trap density or create a surface potential to keep the charge carriers away from the surface. Crystal growth resulting in fewer electronic defect states (typically $<1 \times 10^{15}\ \mathrm{cm}^{-3}$) and elimination of detector fabrication damage also reduces l/f noise. A well-designed detector is dominated by g-r noise associated with random carrier generation and recombination in the semiconductor. The minority carrier lifetime, τ, determines the extent of the g-r noise plateau. Trapping mechanisms, whether bulk or surface, exhibit behavior similar to the g-r process when the trapping time determines the detector response time. Careful analysis is required to distinguish between recombination and trapping. This identification helps in determining the nature of the defect such as the identity of the impurities. For example, copper atoms in HgCdTe reduce the lifetime and detector responsivity. Characterized by τ, the g-r or trapping noise declines as the inverse of frequency and the system or Johnson noise (JN) becomes dominant at the higher frequencies. In general, noise components, V_{i}, are not correlated adding in quadrature to give the total noise as follows:

$$i_N^2 = V_{\mathrm{f}}^2 + V_{\mathrm{g-r}}^2 + V_{\mathrm{JN}}^2 + V_{\mathrm{AMP}}^2 \qquad (6)$$

The noise is expressed as noise density in units of $\mathrm{V/(Hz)^{1/2}}$, or integrated over a frequency range and given as V rms. Typically, photoconductors are characterized by a g-r noise plateau from 10^3 to 10^5 Hz. Photovoltaic detectors exhibit similar behavior, but the l/f knee may be $<$ 100 Hz and the high frequency noise roll-off is determined by the p–n junction impedance–capacitance product or the amplifier (AMP) circuit when operated in a transimpedance mode. Bolometers exhibit an additional noise, V_{TC}, associated with thermal conductance.

3.3. Detectivity

Detector sensitivity (1, 2) is expressed in terms of the minimum detectable signal power or noise equivalent power (NEP) given in units of W or $\mathrm{W/Hz^{1/2}}$. The reciprocal function when normalized for detector area, A, and noise bandwidth, Δf, is defined as detectivity, $D*$, in units of $\mathrm{cm{\cdot}Hz^{1/2}/W}$. Thus,

$$\mathrm{NEP} = \frac{V_N}{R_V} \qquad \mathrm{W\ or\ W/\sqrt{Hz}} \qquad (7)$$

$$D^* = \frac{R_V\,(A\,\Delta f)^{1/2}}{V_N} \qquad \mathrm{cm\,\sqrt{Hz}/W} \qquad (8)$$

The rms noise is measured in a noise bandwidth, Δf. The parameter $D*$ is called D star lambda when the spectral band is limited to a given interval, and $D*$ blackbody when the total blackbody incident power density is used in the calculation.

The blackbody method of calibrating photodetectors is excellent for cutoff wavelengths $>$ 2 μm, but for short wavelength detectors such as visible sensing charge-coupled devices the unit of lux is the scattered illumination power density of 100 $\mu\mathrm{W/cm^2}$ in the visible spectrum. Most CCD cameras have a sensitivity of 3–10 lx. Spatial resolution and image display is often a problem with arrays of discrete detectors because the small objects are undersampled. The results are Moiré patterns and loss of detail. Scanning arrays use overlapping detector geometries to improve the spatial quality of the image. Infrared detector element size is limited to $> 10\ \mu$m by electrical contact methods or photolithographic minimum feature size ($1\ \mu$m) for the detectors or readout electronics.

3.4. Ideal Performance and Cooling Requirements

Free carriers can be excited by the thermal motion of the crystal lattice (phonons) as well as by photon absorption. These thermally excited carriers determine the magnitude of the dark current, J_d, and constitute a source of noise that defines the limit of the minimum radiation flux that can be detected. The dark carrier concentration is temperature dependent and decreases exponentially with reciprocal temperature at a rate that is determined by the magnitude of E_g or E_i for intrinsic or extrinsic material, respectively. Therefore, usually it is necessary to operate ir photon detectors at reduced temperatures to achieve high sensitivity. The smaller the value of E_g or E_i, the lower the temperature must be.

The operating temperature depends on the required sensitivity and the temperature dependence of the various thermal–noise components. In all cases, a practical limitation in sensitivity is imposed by an amplifier or recording device. Theoretical performance can be calculated, assuming that the amplifier noise is negligible as compared with detector noise. Optimum or ideal detector performance is based on the assumption that the detector noise is determined only by the random fluctuations of the photon-absorption process. This ultimate limit on performance can be calculated easily and is used as a final measure of performance for ir detectors (14). For example, consider a photodetector as a photon counter, such as a photodiode connected to an integrating amplifier. After a time interval, Δt, the integrated charge density, Q, may be expressed by the following:

$$Q = \left(J_\phi + J_d\right)\Delta t \qquad (9)$$

The number of integrated carriers, N, is QA/q, where q is the electron charge. Because dark current, J_d, is a combination of thermal excitation processes, neglecting avalanche and tunneling, ideal performance occurs when the photon-induced current density J_φ; is $> J_\mathrm{d}$. Fluctuations of N are the dominant causes of noise. The cooling requirement may be calculated for each type of photon detector by analyzing the dark current noise mechanism in terms of thermal equilibrium processes and setting $J_\phi \geq J_d$ with $J_\phi = \eta\phi q$ A/cm^2 and φ is the sum of the signal and background photon flux. Because the charge density of a photon-counting detector is sampled at time intervals, Δt, the number of charges sampled $N = \eta\phi A\Delta t$.

The generation of photons obeys Poisson statistics where the variance is N and the deviation or noise is $N^{1/2}$. The noise spectral density, N_S, is obtained by a Fourier transform of the deviation yielding the following at sampling frequency, f.

$$N_S = \left(\frac{2N\Delta f}{f}\right)^{1/2} = \left(\frac{2\eta\phi A\Delta t\Delta f}{f}\right)^{1/2} \qquad (10)$$

The signal S, in electrons, is that portion of N that is generated by a signal flux, φ_S, in the same time interval, Δt. Therefore,

$$S = \eta\phi_s A\Delta t \qquad (11)$$

The ideal detectivity may be obtained by combining equations 5, 8, 10, and 11. When $\Delta t = f^{-1}$, the ideal spectral detectivity (2) in cm·Hz$^{1/2}$/W for a photon limited process becomes

$$D_\lambda^* = \frac{\lambda}{hc}\left(\frac{\eta}{2\phi}\right)^{1/2} \qquad \mathrm{cm}\sqrt{\mathrm{Hz}}/\mathrm{W} \qquad (12)$$

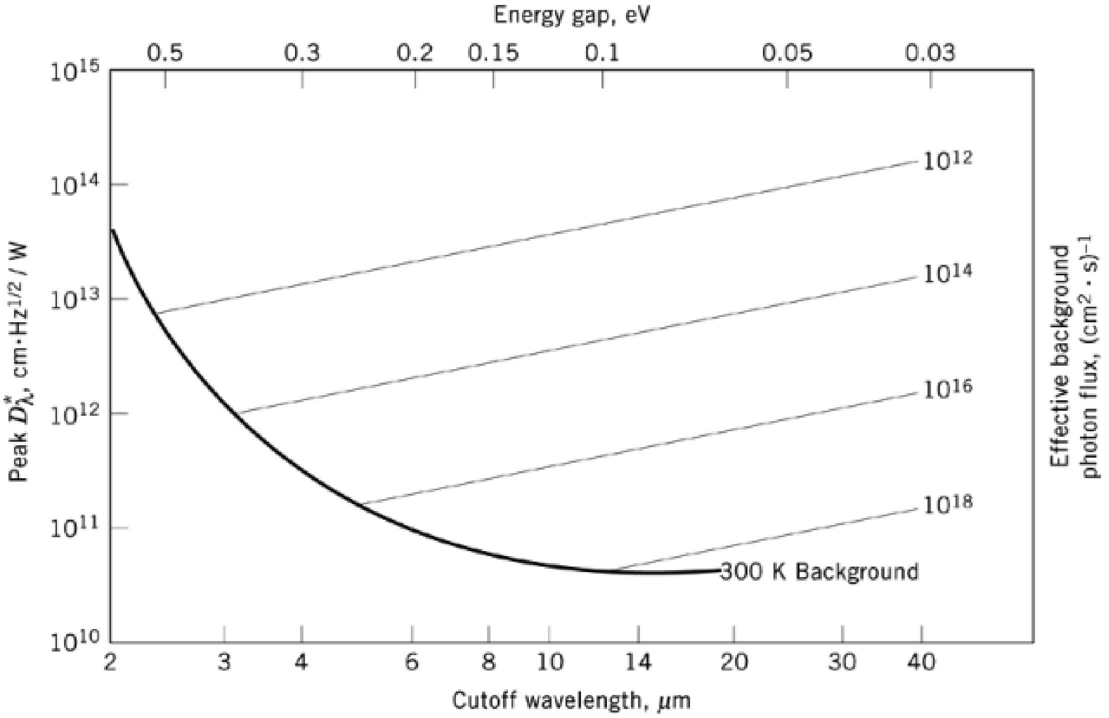

Fig. 3. Ideal photon detector sensitivity as a function of cutoff wavelength. Lower background flux generates less photon-induced noise giving higher sensitivity. The sensitivity limit for the condition of 300 K background temperature and hemispherical (2π) field of view is shown.

When equation 12 is valid, the detector is said to be a background-limited IR photodetector (BLIP). When this is the case, attempts often are made to improve $D*$ by cold shielding which reduces φ. The ideal $D_\lambda{}^*$ is shown in Figure 3 as a function of wavelength with background photon flux as a parameter. The line of termination in the lower left corner represents $D_\lambda{}^*$ values for a 180° (2π) detector field of view, 300 K ambient background temperature, and background emissivity $\epsilon = 1.0$. As long as the photon-generated current exceeds the dark currents, $D_\lambda{}^*$ may be increased by reducing the background flux. For very low values of photon flux, the ideal detection condition of equation 12 can be restored by cooling the detector to decrease the dark currents.

The cooling needed to achieve a given detectivity for intrinsic-type detectors may be readily calculated based on the temperature dependence of the minority carrier lifetime and mobility. The calculated values for indium arsenide [1303-11-3], InAs [1303-11-3], and two compositions of HgCdTe, are given in Figure 4. Experimental data for lead sulfide [1314-87-0], PbS [1314-87-0], and three HgCdTe detectors having different compositions, are also shown. The importance of cooling is obvious.

Detector cooling often is accomplished by providing good thermal conductivity to a suitable cryogen (2). The most readily available coolants are solid carbon dioxide [124-38-9], CO_2 [124-38-9], at 195 K, liquid nitrogen, N_2, at 77 K, and liquid helium, He, at 4.2 K. If the desired temperature is not below $\sim$ 200 K, a thermoelectric cooler may be used. Joule–Thompson and expansion engine coolers are available for operation to 4.2 K and below. A cooled detector must be contained in a vacuum vessel that thermally isolates the detector element from other than the coolant by low thermal conduction materials and vacuum. If low absorbing extrinsic detectors are used, it is customary to enclose the detector element in a cooled chamber with reflecting walls, ie, in an integrating chamber, in order to obtain multiple passes of the radiation. The latter also can be accomplished by

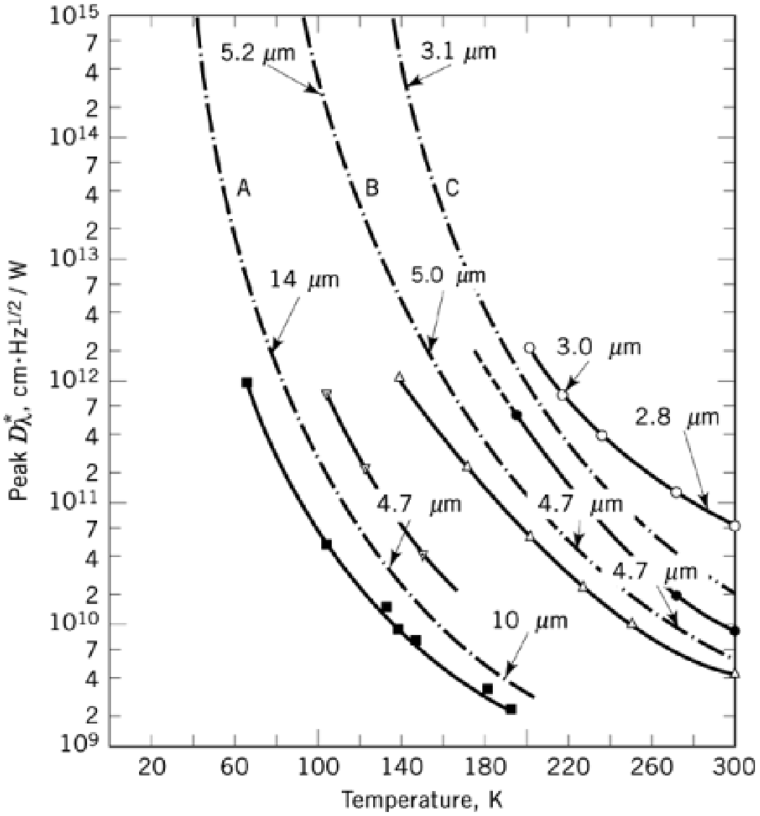

Fig. 4. Sensitivity as a function of detector temperature showing (—) experimental results for HgCdTe; (■ and △) $Hg_{1--x}CdTe$, $x=0.185$ and $x=0.280$, respectively; (▽) InSb; (•) InAs; and (◦) PbS. Also shown are theoretical values (— • —) based on thermal equilibrium statistics, A and B, $Hg_{1--x}CdTe$ where $x=0.195$ and $x=0.29$, respectively; and C, InAs.

shaping the element so as to ensure multiple, total, internal reflections. Thin detectors can be sized to produce optical resonance in the detector element making the detector itself an optical resonant cavity.

The choice of a detector for a specific application should be made in order to minimize the cooling requirements and the magnitude of the background radiation noise; therefore, in detector selection the cutoff wavelength should be only slightly greater than that required by the application. If the signal radiation has a substantial path length through the atmosphere, then atmospheric transmission characteristics must be considered. Because of the presence of CO_2 and H_2O vapor, many absorption bands appear in the atmospheric transmission spectrum. Windows of high transmittance occur between the bands. The principal windows are at 1.0–2.5, 2.9–4.2, 4.4–5.3, 7.5–14.0, and 16–23 μm (2).

4. Photodetector Modes of Operation

The need for detectors with high performance and low cost has resulted in < 24 types of detectors that are available as commercial products. These are made from only 10 basic semiconductor elements or compounds. Popular detectors, their modes of operation, cutoff wavelength, temperatures of operation, response times, responsivities, and detectivities are listed in Table 1 (15). The values chosen are for near-optimum performance at a given temperature. Silicon-based photon detectors, such as photovoltaic and charge-coupled detectors operate near room temperature. Cadmium sulfide [1306-23-6] and germanium detectors also require no cooling. Wide acceptance of the ternary compound semiconductor mercury–cadmium–telluride [29870-72-2] (MCT), HgCdTe, began in 1972 as a photoconductor. Requirements for large focal planes has since led to significant developments of the MCT photodiode focal plane (16). The controllable (by composition) band gap of MCT in each case results in a cutoff wavelength that is tailored for a specific application (see Fig. 4). Lead sulfide, indium arsenide, and MCT (40% at. wt CdTe) detectors can be operated at 300 K but perform much better at lower temperatures (2, 14).

Four principal modes of semiconductor-based photodetectors are the photoconductor, photodiode, charge-mode device, and bolometer. The Schottky barrier mode using internal photoemission has been well developed using platinum silicide, but low quantum efficiency restricts the range of uses. The quantum well infrared photodetector (QWIP) is included herein because artificially structured materials such as this superlattice detector are representative of a new metallurgy. The semiconductor materials for most applications are Si, Ge, GaAsP, InSb, PbS, CdS, and HgCdTe. These materials grown as single crystals and thin polycrystalline or amorphous films are doped with various elements such as boron, phosphorus, indium, gold, etc, to control the polarity of the conductivity and for selective optical absorption by the introduction of impurity states in the forbidden energy gap. Photodetection using these materials extends from the ultraviolet (0.3 μm) to long wavelength ir (200 μm). Higher sensitivity, especially in the ir, can be achieved by cooling the detector and its immediate surroundings to low temperature, typically 77 K. Interfacing with signal processing electronics can be difficult when the photon signal is weak and imaging systems require sophisticated signal processing to handle the hundreds of thousands of pixels on a focal plane.

4.1. Photoconductors

The photoconductor (17) is a semiconductor resistor that lowers in resistance when photons generate excess carriers. The two general classes of photoconductor are extrinsic, which is characterized by impurity states that are emptied by photons, and intrinsic, where the photons excite electrons directly from the valence band to the conduction band (Fig. 1). The photoconductor is connected in series with a constant load resistor and current source. The ambient light or background radiation sets up a steady-state resistance in the detector. Changes in illumination produce changes in resistance and thereby changes in the voltage across the load resistor. When the load resistance is much larger than the detector resistance, signal voltage is given by equation 13:

$$V_S = \frac{\eta \phi_s \tau V}{nt} \qquad (13)$$

where the signal flux, φ_s, is caused by the changing background. At low bias the signal is linear with the bias voltage, V, but at high bias the minority carrier sweep time becomes less than the lifetime, τ, and the signal saturates. The majority carrier density, n, is typically 1×10^{15} to $1 \times 10^{16}/\text{cm}^3$. The thickness, t, is typically one to three absorption lengths (8–20 μm).

4.2. Photodiodes

Photovoltaic detectors (17) generate a voltage (open circuit) or a current (closed or integrating circuit) when receiving radiation and therefore do not require an external bias for operation. The charge integrated on a capacitor of the integrating circuit is proportional to the intensity of radiation. The current generated by the photovoltaic cell, I_s, is given by the following.

$$I_s = \eta \phi_s q A \qquad (14)$$

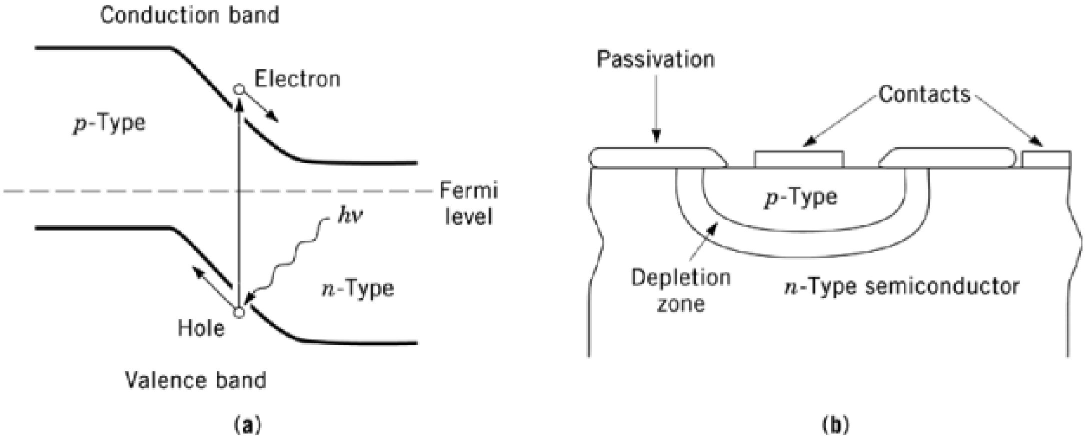

Fig. 5. The photodiode detector: (**a**) band model where the photon generates electron–hole pairs that are separated by the built-in potential setting up a photocurrent; (**b**) physical model for a planar diode. The passivation is typically SiO_2 for Si diodes, an In oxide for InSb diodes, and CdTe for HgCdTe diodes.

The quantum efficiency can be determined using the measured current and the aid of a calibrated photon source, eg, a blackbody. The detector area, A, should be measured by a spot-scanning apparatus, because the minority carrier diffusion length effectively increases the diode photon-active area. A photovoltage can arise from the presence of internal fields that are formed at the interface between a semiconductor and a metal (Schottky) barrier, at the interface between different dopings in a semiconductor (homojunction), and at the interface between two different semiconductors (heterojunction). Light releases mobile electric carriers within these barrier layers. These carriers are separated by the field and produce a photovoltage between them, as indicated in Figure 5. Photovoltages can be produced in the bulk of a semiconductor because of the difference in the diffusion of electrons and holes or if there is a gradient in the impurity concentration within the material, but these mechanisms are not in wide use.

The impedance area product, *ZA*, of a diode may be obtained from differentiation of the diode current–voltage relationship and may be expressed as follows, at zero applied basis.

$$ZA = \frac{kT}{BqJ_d} \qquad (15)$$

Under little or no illumination, J_d must be minimized for optimum performance. The factor B is 1.0 for pure diffusion current and approaches 2.0 as depletion and surface-mode currents become important. Generally, high crystal quality for long minority carrier lifetime and low surface-state density reduce the dark current density that is the sum of the diffusion, depletion, tunneling, and surface currents. The *ZA* product is typically measured at zero bias and is expressed as R_0A. The ideal photodiode noise current can be expressed as follows:

$$i_N^2 = 2qA\left(2J_d + J_\phi\right)\Delta f \qquad (16)$$

where J_φ; is the photon current density. Equations 15 and 16 can be used to determine the cooling requirements for photodiode detector performance since diffusion current depends exponentially on temperature (18). Because the diffusion current represents a valence band-to-conduction band excitation, the thermal limit, when $J_d > J_\phi$, is essentially the photoconductive limit (see Fig. 4). Combining equations 5, 8, 14, 23, and 24 gives the

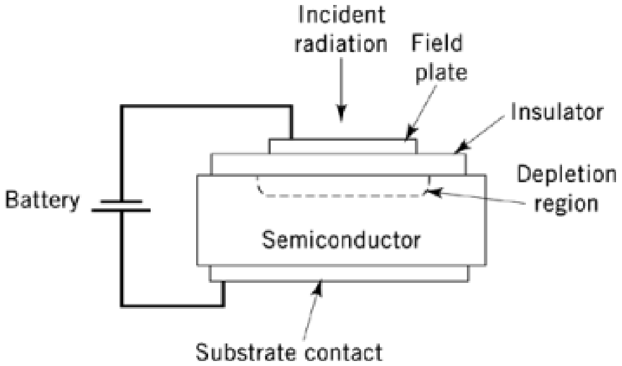

Fig. 6. Device model for an MIS photodiode, the basic building block of the CCD photodetector. The depletion region is generated by the battery potential. See text.

following:

$$D^* = q\eta/h\nu\left(4kT/ZA + 2qJ_\phi\right)^{1/2} \qquad (17)$$

Thus, ZA must be increased to achieve BLIP $D*$ such that $ZA > 2\,kT/qJ_\phi$. When $J_\phi > J_d$, equation 17 reduces to the ideal photon limit of equation 12. The response time is equal to the ZC product, where C is the diode capacitance, or when using an integrating amplifier, the response time is determined by the closed loop gain.

4.3. Charge Mode Detector

Charge mode devices (19, 20) are a group of detectors that utilize the metal–insulator–semiconductor (MIS) capacitor as their basic constituent. An MIS capacitor is a device consisting of a nondegenerately doped semiconductor substrate, a thin dielectric layer, and a metal gate, as shown in Figure 6. The application of a potential difference across the metal gate and the semiconductor produces a surface potential barrier and an associated depletion region in the semiconductor. Periodic pulsing of the gate-to-substrate bias creates a nonequilibrium condition suitable for the storage of optically generated free carriers.

The model for an MIS capacitor is shown in Figure 7 and includes a metal gate–to–semiconductor bias of V_g volts producing an insulator bias, V_I, and surface potential, Ψ_s. The negative for n-type material gate charge, Q_s, produces an ionic space charge, Q_d, and inversion layer charge, Q_p. From the basic relationships (21) that follow,

$$V_g = V_I + \Psi_s \qquad (18)$$

$$Q_s = Q_d + Q_p \qquad (19)$$

where $Q_s = C_I V_I$ and $Q_d = C_d \Psi_s$ then

$$\Psi_s = V_g/(1 + C_d/C_I) \qquad (20)$$

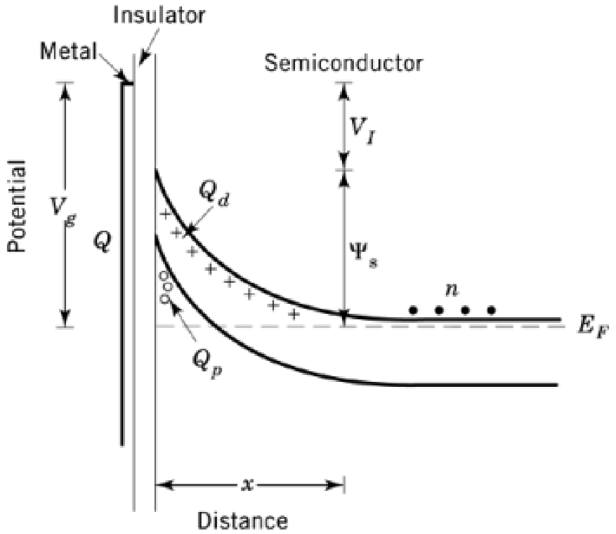

Fig. 7. Band model for the charge mode detector biased to deep depletion. The charge, Q_p, integrates in the potential well defined by the insulator and valence band. See text.

where C_d is the capacitance associated with the space–charge layer geometry of charge n at distance x. From semiconductor theory,

$$\Psi_s = nqx^2/2\epsilon \qquad (21)$$

where ϵ is the dielectric permittivity of the semiconductor and, from geometry,

$$C_d = \epsilon A/x \qquad (22)$$

The basic MIS condition is obtained by combining equations 18–22:

$$\Psi_s + (\epsilon qn/2)^{1/2} A(\Psi_s)^{1/2}/C_I = VQ_p/C_I \qquad (23)$$

At initial turn-on, the inversion charge $Q_p = 0$ and when n is small and C_I is large, $\Psi_s = \mathrm{ca}\ V$, that is, a potential well of nearly V is formed. Thus, the charge-handling capacity, Q_FW, is

$$Q_\mathrm{FW} = \mathrm{ca}\ C_I V \qquad (24)$$

and can be seen to be dependent on both the physical dimensions of the capacitor and the applied voltage. Typical full well (FW) capacities range from 10,000 carriers to > 5,000,000 carriers, depending on the specific charge mode device.

As time progresses, charge Q_p is generated by photon currents, semiconductor dark currents, diffusion, depletion, surface, avalanche, and tunneling. The time required to fill the well by dark currents is the storage time, τ_{st}, given by the following.

$$\tau_{st} = C_I V/J_{dark} \qquad (25)$$

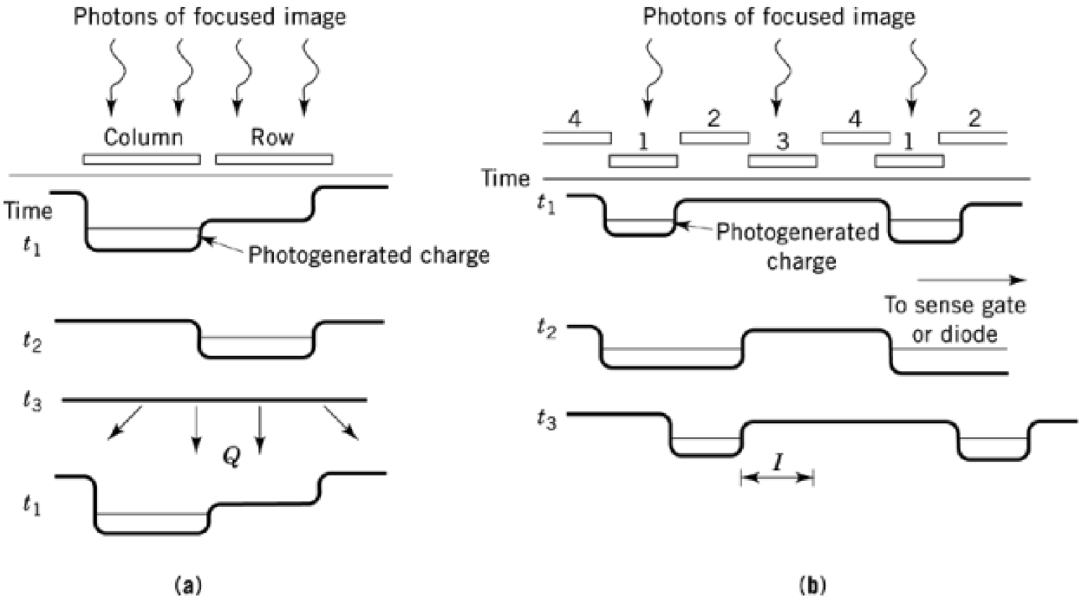

Fig. 8. Conceptual cross-section views of (**a**) a CID imager showing charge integration (t_1), charge measurement (t_2), and charge removal (t_3); and (**b**) a CCD shift register showing charge transfer from a phase one well to a phase two well.

The storage time is the maximum time the potential well can be used for collection of photon-generated charge. Because J_d depends strongly on band gap energy and temperature of operation, τ_{st}, in practice, extends from hours for silicon at 300 K to a few microseconds for HgCdTe, where the cutoff wavelength, $\lambda = 12\ \mu\mathrm{m}$ at 77 K. Indium anitmonide operates in a few tenths of a second at 77 K (22).

As previously indicated, the MIS capacitor can be utilized as a photon detector. A negative pulse on an n-type semiconductor generates a deep depletion region at the surface which, in turn, acts as a storage site for photogenerated holes. This type of detection is true charge integration and is the simplest charge mode detection concept. Other MIS devices exist that contain arrays of overlapping, ie, metal gates in a given detector element. These MIS-based detectors are called charge-transfer devices (CTD). The two most common forms of CTDs are charge-injection devices (CID) and charge-coupled devices (CCD).

The CID is a dual gate version of a CTD. In the CID, two gate electrodes form two distinct but physically adjacent depletion capacitances, as shown in Figure 8**a**. Under normal operating conditions each of the two gate electrodes is biased to form a depletion region in the underlying semiconductor. However, the surface potential minimum under one of the electrodes is much greater than that of the other electrode. As a result, the photogenerated charge produced in the detector collects in the deeper potential minimum. To measure the number of stored carriers, the potential difference between the collection electrode and the semiconductor substrate is reduced, thereby collapsing the storage well and forcing the collected charge to transfer to the region controlled by the second gate electrode. The collected charge can, in principle, be quantified by monitoring the change in surface potential of this second electrode during the transfer operation. In practice, this is accomplished by monitoring the instantaneous current through the electrode at the instant of charge transfer. The detector is reset to the empty state by simultaneously collapsing the depletion regions of both capacitors. This action forces the free carriers into the semiconductor substrate where they are subject to recombination mechanisms. Thus a key feature of a CID is that photogenerated charge is both collected and sensed inside a single detector element. Signal charge is transferred from that element simply as a means to eliminate it from the detector prior to the next detection cycle.

The CCD is a multigate CTD. As for the CID, the CCD gates are physically adjacent and are periodically pulsed, inducing the formation of deep depletion regions in the underlying semiconductor. However, unlike the CID, the CCD physically transfers the collected photogenerated charge from a given detector site to a separate charge measurement structure. Figure 7**b** shows a conceptual cross-section view of a CCD shift register. As the photons of an image that is focused on the device generate charge, the MIS gates of the shift register are biased in sequence to produce, continually, a shifting potential well pattern. Thus, at time t_1, phase one is on and charge is integrating in the potential well beneath the MIS phase one gates. At time t_2, phases one and two are turned on and the charge distributes beneath phase one and phase two gates. At time t_3, phase one is turned off and the charge is beneath phase two only. Pulsing phases three and four in the proper sequence with phase one and two moves the charge packet through the shift register. For an area array CCD the imaging portion of the array transfers charge, once per line interval, into a readout shift register in a manner equivalent to that described for the imaging shift register. Each charge packet in the imaging register is then shifted in a discrete fashion to the charge-detection structure residing at the end of the register. This sense electrode or diode is in turn typically connected to a low noise charge-sensitive amplifier that converts the signal charge to a voltage. After all charge packets in the shift register have been read out, the next line of information from the imaging portion of the array is transferred and the process is repeated.

4.4. Bolometers

The bolometer (23) has made a comeback as a popular detector thanks to advances in micromachining technology. When applied to silicon it is feasible to fabricate large arrays of bolometers and detecting elements having very small thermal mass. The imaged ir radiant power slightly heats the bolometer film a few millidegrees kelvin causing a lowering of the electrical resistance. The resulting change of the bias current is the signal. The noise components are l/f, Johnson thermal conductance, and photon. The photon noise is actually the radiative part of the thermal conductance noise.

From bolometer theory (1) the change in film temperature is proportional to the absorbed power and thermal resistance (inverse of the thermal conductance) and is given by the following:

$$\Delta T_b = \Delta J A \epsilon_a R_{th} \frac{\left(1 - \exp\frac{-\tau_s}{R_{th}C_h}\right)}{\left(1 + \exp\frac{-\tau_s}{R_{th}C_h}\right)} = \Delta J A \epsilon_a R_{th} \tanh\left(\frac{-\tau_s}{2R_{th}C_h}\right) \qquad (26)$$

where ΔJ is the differential power density at the detector caused by a change in target temperature in W/cm^2; A is the active pixel area, $1.2 \times 10^5\ \text{cm}^2$; ϵ_a is the IR absorption efficiency, 90%; R_{th} is the thermal resistance and is $\sim 1.5 \times 10^7\ \text{K/W}$; τ_s is the half-period of chopped radiation ($1/2 f_c$), typically 16.7 ms (30-Hz modulation); and C_{h} is the heat capacity of the pixel element and is approximately $0.7 \times 10^{-9}\ \text{J/K}$.

The power density, J_{s}, may be calculated using Plank's radiation law. For a 300 K scene temperature and the spectral region from 8 to 12 μm,

$$J_s = 2.0\ E - 4\left(\epsilon_0 \Delta T_s \frac{\Omega}{\pi}\right) \qquad (27)$$

where ϵ_0, the optical efficiency, is typically 80%, ΔT_{s} is the differential target temperature, and Ω is the collection solid angle of the optical system $[=\pi \sin^2(\tan^{-1} 1/2 f_n)]$.

For the bolometer detector having the above characteristics and operating with $f/1$ optics ($f_n = 1$) the peak to peak temperature change of the α-Si film is approximately 3 mK/1 K change in scene temperature.

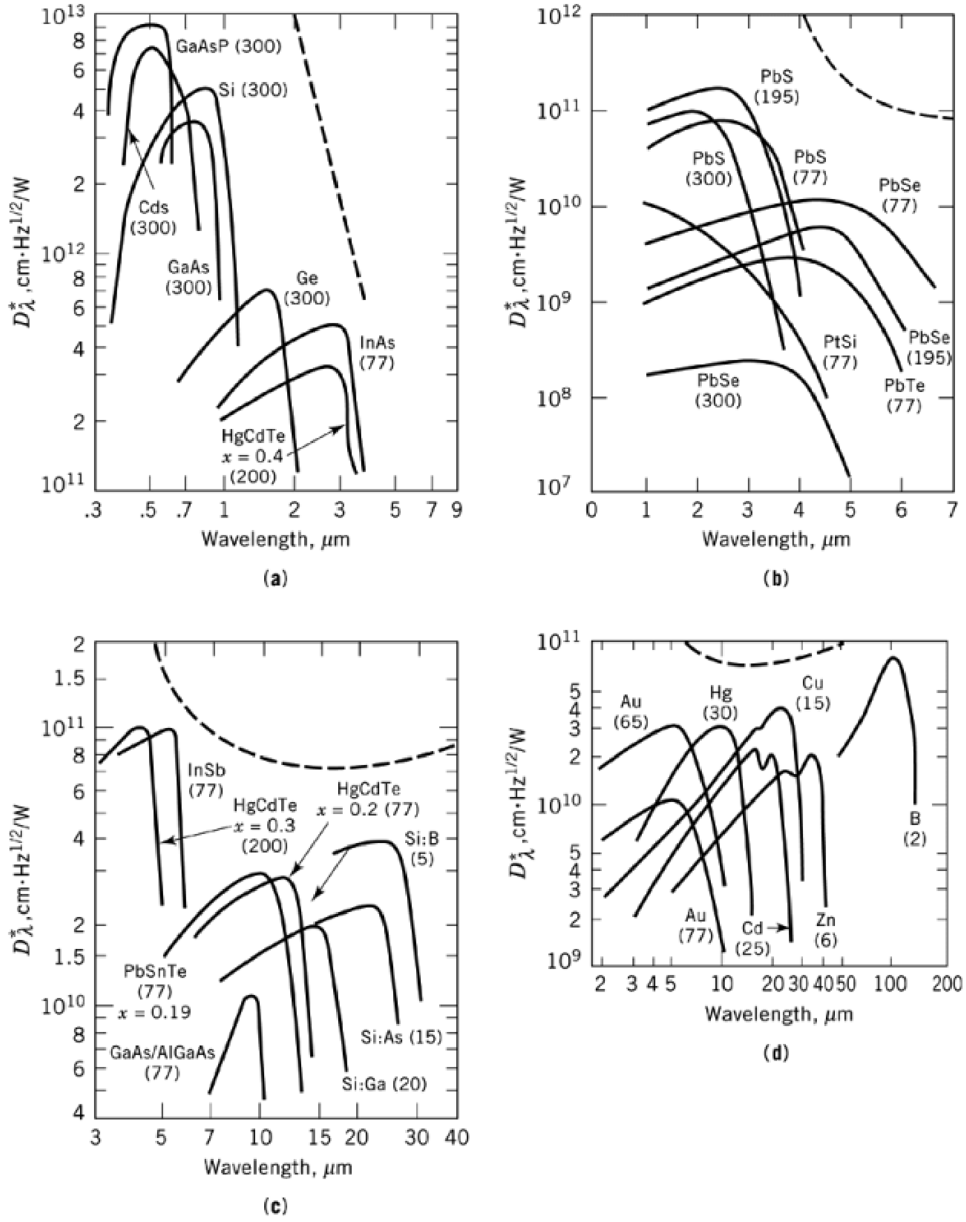

Fig. 9. Spectral sensitivity of detectors where the detector temperatures in K are in parentheses, and the dashed line represents the theoretical limit at 300 K for a 180° field of view. (**a**) Detectors from near uv to short wavelength ir; (**b**) lead salt family of detectors and platinum silicide; (**c**) detectors used for detection in the mid- and long wavelength ir. The Hg_{1--x}CdTe, InSb, and PbSnTe operate intrinsically, the doped silicon is photoconductive, and the GaAs/AlGaAs is a structured superlattice; and (**d**) extrinsic germanium detectors showing the six most popular dopants.

4.4.1. Signal

The peak-to-peak signal voltage, V_s, is proportional to the bias power and can be expressed as follows:

$$V_s = \alpha\,(PR_b)^{1/2}\,\Delta T_b \qquad (28)$$

where α is the temperature coefficient of resistance and is 2.8%/K for α-Si, P is the bias power for the bolometer element (typically 0.3 μW), and R_b is the bolometer resistance (typically $3 \times 10^7\ \Omega$ for α-Si and $1 \times 10^4\ \Omega$ for VO).

The voltage responsivity is simply given by equation 29:

$$R_V = \frac{V_s}{J_s A} = \alpha\,(PR_b)^{1/2}\,\epsilon_a R_{th} \tanh\left(\frac{-\tau_s}{2\,R_{th} C_h}\right) \qquad (29)$$

Responsivity values are typically $5 \times 10^5\ \mathrm{V/W}$ range for nominal bias.

4.4.2. Noise

The noise components may be expressed as voltage. Excess (l/f) noise:

$$V_f = \int_{\Delta f} \left(\frac{\gamma}{f^{1/2}}\right)^2 df = K_V\,(PR_b)^{1/2} \qquad (30)$$

where K_V is the l/f noise coefficient and is typically in the range from 6 to 12 μV per volt bias when integrated from 1 to 100 Hz. Johnson noise, V_JN, is

$$V_\mathrm{JN} = (4kTR_b\Delta f)^{1/2} \qquad (31)$$

where k is the Boltzmann constant, T is the detector temperature (300 K), and Δf is the noise bandwidth (100 Hz). Thermal conductance noise, V_TC, is

$$V_\mathrm{TC} = \alpha\,(PR_b)^{1/2}\left(\frac{kT^2}{C_h}\right)^{1/2} \qquad (32)$$

when the thermal response time $R_\mathrm{th}C_\mathrm{h}$, is less than the frame time.

4.4.3. NEP

The noise components may be combined with the responsivity to give the NEP equation:

$$\mathrm{NEP} = \frac{\left(V_\mathrm{JN}^2 + V_\mathrm{EX}^2 + V_\mathrm{TC}^2\right)^{1/2}}{R_V} \qquad (33)$$

Measured values are typically < 100 pW for a 30-Hz scene modulation.

5. Detector Fabrication and Performance

Significant improvements in detector performance and focal plane array development have occurred since the early 1980s (24, 25). The spectral sensitivities of several photodetectors are given in Figure 9 covering the spectrum from uv to far ir. The typical operating temperature is given and the theoretical limit is that calculated for the detector exposed to hemispherical radiation from a 300 K background.

5.1. Charge-Coupled Devices and Imaging Arrays

The single most popular type of visible photon detector is the CCD. Developed in 1970 (26, 27) as a dynamic memory storage device, the CCD was quickly adapted for use as an imaging device. The CCD has been a resounding commercial success, becoming the detector of choice in the video camera market, and demonstrating great potential as the optimum detector for future electronic still photography (qv) systems. Furthermore, since its inception the CCD has also been an invaluable tool in a wide range of scientific applications involving the detection of near-ir, visible, uv, and X-ray photons, as well as in the detection of ionizing radiation and charged particles.

CCDs are sensitive photon detectors. The physical mechanism governing photon detection in silicon depends on the energy of the incident photons. For the near-ir to visible spectral band, silicon performs as an indirect band gap semiconductor. Incident photons are converted to electron–hole pairs through interactions with the silicon lattice, producing one electron–hole pair for each absorbed photon. For higher energy photons such as those of the extreme uv and X-ray spectral bands, direct band gap detection dominates. In this case, one electron–hole pair is generated for every 3.65 eV of energy contained in the absorbed photon. If the scene of interest produces only a small number of high energy photons impinging on the detector array during each frame interval, the number of signal electrons in each pixel is a measure of the energy of the incident photon. In such applications, CCDs can be used to obtain spectral as well as spatial information (28).

5.1.1. Utilization

CCDs are often grouped into two broad categories: commercial grade and scientific grade. For both categories the format and required performance of the CCD are driven by the application for which the array is designed. In general, commercial grade CCDs are designed to optimize image resolution and color fidelity. On the other hand, scientific grade CCDs are designed to maximize photon quantum efficiency and minimize device noise. The vast majority of available CCDs have been designed for commercial applications. By virtue of the relatively small number of devices that are supplied yearly for scientific applications, and the more stringent performance requirements, scientific grade CCDs are typically more expensive than their commercial counterparts. Commercial grade CCDs can be adapted for use in scientific applications where a moderate photon level is present, such as some forms of visible spectroscopy.

Most CCDs are specifically designed for video camera applications, which detect photons in the visible portion of the electromagnetic spectra. Video camera CCDs have specific camera formats compatible with standard video display systems. In the United States, video displays utilize the RS-170 standard, commonly known as the National Television System Committee (NTSC) 525-line television standard. The RS-170 standard places many constraints on imaging devices. These devices must have a frame time of 1/30 s, with two interlaced image fields of 1/60 s each required during each frame. The standard luminance electrical bandwidth of 4.2 MHz coupled with the 4:3 picture aspect ratio require the pixel count and the pixel size of the commercial CCD array to fit within narrowly defined regimes. Specifically, to meet the electrical bandwidth requirements of the RS-170 standard, monochrome imagers must have a minimum of 240 pixels in the vertical dimension and a minimum of 450 pixels in the horizontal dimension. The distance along the diagonal of the active imaging portion of the CCD must be one of several specific values in the 5.46–25 mm range. The specific value depends on the particular camera format, eg, 8 mm, VHS, etc, for which it is designed. These format and size requirements dictate a rectangular rather than square CCD pixel design. Data rates from the imaging devices must be chosen so that the image scene readout time matches the RS-170 interval. The minimum data rate for monochrome imagers is 6 MHz. The actual rate spans from 6 to 10 MHz, depending on the specific device.

Color applications require more complex image detection schemes owing to the need for spectral differentiation. Signal samples from at least three distinct spectral bands are required to accurately reproduce a color image. Typically a monolithic color filter array consisting of alternating windows of appropriately colored filter media is attached to the CCD to accomplish color differentiation. A common approach to obtain the scene information required for faithful color image reproduction is to increase the horizontal pixel count of the CCD by a factor of three (29). In this method, a filter with alternating red, blue, and green stripes is then attached so that each pixel column aligns with a filter stripe. This color CCD utilizes three adjacent pixels, one red, one green, and one blue, to represent a single spatial sampling of the scene. In effect, the device can be thought of as three integrated monochrome CCDs. The color CCD has three on-chip output channels, one for each spectral component. As each pixel is read, the simultaneously generated signal information from each channel is remixed in a fashion that correctly simulates a color display. More ambitious methods exist for achieving color image reproduction (30, 31). These methods utilize the horizontal pixel count found in monochrome CCDs but require intricate clock control methods to appropriately intermix the spectral components for display during the actual integration interval. The intermixing is produced by the use of a repetitive mosaic pattern of colored filters, typically cyan, yellow, and green. The imaging results from these devices rival those obtained from the three-channel method.

Video camera applications obligate the CCD imager to have an internal, electronic, image shuttering capability in order to clearly differentiate the data in one image frame from that of the next. The two most common forms of internal shuttering are frame transfer and interline transfer (32). In the frame transfer technique, the image gathered from one data frame is rapidly transferred from the contiguous image collection region to a secondary, optically shielded storage site that resides between the image collection and shift register regions. The image held in the shielded region is then read out during the time interval of the next image formation in the optically active area. In the interline transfer technique, each pixel in the imaging portion of the array is segmented into an optically active portion and a shift register portion. The image gathered from one data frame is quickly transferred from the optically active to the shift register portion of the pixel, and read out during the next image collection interval. Unlike the frame transfer method, no additional image storage section is required for the interline transfer method. However, the frame transfer device is more efficient at photon detection, since there are no optically shielded features in the image collection region.

Most CCDs for consumer applications are illuminated from the front surface of the device. Photons impinging upon the front surface of the detector must pass unimpeded through the gate electrode layers in order to be collected in the photon-sensitive silicon beneath. Typically, some loss does occur for photons of wavelengths shorter than $\sim$ 550 nm due to absorption in the gate electrodes. For standard polysilicon gate CCDs, photons of wavelength $<$ 400 nm are absorbed by the gate material. This absorption process affects photons spanning the uv to low energy X-ray spectrum. Photons of wavelengths $>$ 650 nm pass easily through the gate electrodes, but owing to the lower value of the absorption cross-section of silicon, a several micrometer path length is required to provide a high probability of absorption. Deeply generated signal charge can produce image smearing due to charge diffusion prior to collection in the potential well of the CCD pixel. Both the photon collection efficiency and image quality are strong functions of the particular CCD design. Typical consumer-quality CCDs provide sensitivities spanning the 50–500-mA/W range and have minimum detectable signal levels of from 40 to 400 photons at the standard 16-ms image integration interval.

CCDs are widely utilized in the field of electronic still photography. The late 1990s saw the development of a myriad commercial digital electronic camera systems. The quality of these systems spans the range of very low cost, low resolution cameras for internet imagery to very expensive, 35-mm film quality imagery for professional photography. Unlike film-based cameras, images are stored on electronic media such as a floppy or optical disk. The image can be read into a computer-based system, edited, or enhanced as desired, and stored again onto the digital media. Hard copies are obtained by devices ranging from low cost photographic quality color printers for personal computers to separate image transfer systems specifically designed for photographic paper. Still photography places more stringent specifications on a CCD than those required of RS-170 video cameras in terms of both performance and resolution. Matching the image quality of 35-mm film requires a CCD with a format of > 4000 × 4000 pixels capable of faithfully reproducing an image at low light levels. The development of digital photography has raising the performance level of some commercial CCDs to that of custom scientific quality devices.

Whereas some consumer CCDs can occasionally be adapted for scientific endeavors, in general these devices have format and operability constraints that negatively impact their performance in many applications. Scientific CCDs are somewhat more difficult to categorize because of the wide range of capabilities available in such devices. The performance features of a specific scientific CCD are determined by the device design. A few of the more significant performance features that may be found in a given scientific CCD include the following: (1) spectral response extending over a wide range of photon and charged particle energies; (2) noise levels as low as one electron per pixel, which result in very high signal-to-noise ratios; (3) very high charge-transfer efficiencies to achieve no measurable degradation in spatial or spectral information upon image readout; (4) dark current generation rates permitting several minute integration times at room temperature and multiple hour integration times at cryogenic temperatures; (5) high photon detection efficiency; and (6) high frame rate operability. In addition, scientific CCDs are typically operated in the full-frame readout mode (32), in which an external mechanical shutter shields the imager during scene readout.

Scientific CCDs have been used in a wide range of applications. In the visible and UV portions of the spectrum, scientific CCDs have proven to be effective tools for low photon flux applications. Specifically, CCDs have been utilized as image detectors in ground-based telescopes (33, 34) as well as in space-borne systems such as the Wide-Field Planetary camera of the earth-orbiting space telescope (35, 36), the Giotto mission to Halley's comet (37), and the Galileo mission to Jupiter (38, 39), and the Cassini mission to Saturn (40). Figure 10 is a photomicrograph of the a photomicrograph of a 6-in. diameter silicon wafer containing over a dozen different varieties of scientific CCDs. The wafer contains a 4096×4096 pixel device for astronomy, several 1024×2048 pixel imagers for slow scan frame store operation, a 1024×1024 element CCD for use in very high speed image acquisition, and numerous other imager types. The photomicrograph was taken from a complete Si wafer after device processing but prior to device packaging.

The same features that make scientific CCDs excellent devices for astronomy, that is, high photon collection efficient and low readout noise, also make CCDs excellent tools for chemical analysis (41). CCDs can be utilized in many forms of spectroscopy (42), including absorption (43, 44), fluorescence (45–47), luminescence (48, 49), emission (50–52) and Raman (53–55), over a spectral range of 0.1–1100 nm. The high dynamic range (typically >100 dB) of the CCD is an invaluable property for identifying weak spectral lines. Furthermore, the inherent integration of many highly sensitive photodetector elements in a small area has, in some instances, allowed revolutionary experimental designs (56). Several visible light spectrometer systems that utilize CCDs as the imaging device are commercially available.

In the X-ray portion of the spectrum, scientific CCDs (57, 58) have been utilized as imaging spectrometers for astronomical mapping of the sun (59), galactic diffuse X-ray background (60), and other X-ray sources. Additionally, scientific CCDs designed for x-ray detection are also used in the fields of X-ray diffraction, materials analysis, medicine, and dentistry. CCD focal planes designed for ir photon detection have also been demonstrated in InSb (61) and HgCdTe (62) but are not available commercially.

5.1.2. Fabrication

Although CCDs have been fabricated in many semiconducting materials such as Ge (63), InP (64), and HgCdTe (65), by far the most readily available devices are those that utilize Si as the semiconductor. There are several common types of silicon CCDs. All share certain processing steps, and most utilize *p*-type silicon as the semiconducting material. Silicon single crystals are grown (66) in conventional Czochralski vertical pullers using a single-crystal silicon seed dipped and rotated in a silicon melt. The large boules of silicon are sawed

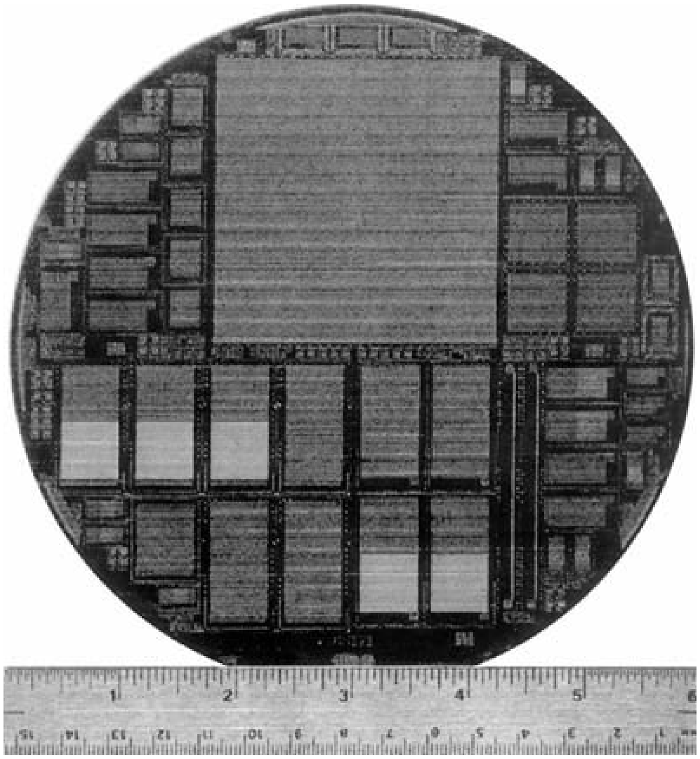

Fig. 10. This mainfigure is a photomicrograph of a 6-in. diameter silicon wafer containing over a dozen different formats of scientific CCDs. Included in the wafer is a 4096×4096 pixel device for astronomy, several 1024×2048 pixel imagers for slow scan frame store operation, and a 1024×1024 element CCD for use in very high speed image acquisition.

into wafers. The following fabrication discussion describes a process for the creation of a generic four-phase CCD in p-type silicon (67).

A cross-section view of a four-phase Si-based CCD is shown in Figure 11. The starting wafer is a thin p-type silicon layer grown epitaxially on a degenerately doped $p+$ silicon substrate of roughly 500-μm thickness. The epitaxial layer is typically 8–15 μm in thickness and is doped with boron to a nominal resistivity of 10 $\Omega\cdot$cm. The initial step of the fabrication process consists of a cleaning procedure designed to ensure a nearly defect-free surface. Next, a thin layer of protective SiO_2 is grown on the silicon surface by the use of elevated temperatures in a steam and oxygen ambient. Channel stops, thin stripes that provide lateral containment of the stored charge, are created by high energy implantation of p-type ions into appropriate regions of the silicon. Most CCDs are designed with a thin layer of n-type dopant at the silicon surface that serves to hold the stored charge physically away from the silicon surface. This dopant layer, called the buried channel, is produced by implanting n-type dopant ions such as P or As into the silicon. After the implantation of the channel stops and buried channel, the original SiO_2 layer is removed and a fresh, undamaged layer is SiO_2 is regrown. Next a layer of heavily impurity-doped polysilicon is deposited and patterned to form the φ_2 and φ_4 gate electrodes. An additional layer of SiO_2 is then grown to provide an effective insulating layer atop the first polysilicon layer. The φ_1 and φ_3 gate electrodes are formed from a second layer of heavily impurity-doped polysilicon. A low resistance material such as aluminum is then used to form electrical connections between appropriate parts of the CCD. Typically this same metal layer is utilized to form bond pads that connect the CCD to external control signals from off-chip electronics. However, some process sequences require the inclusion of a second

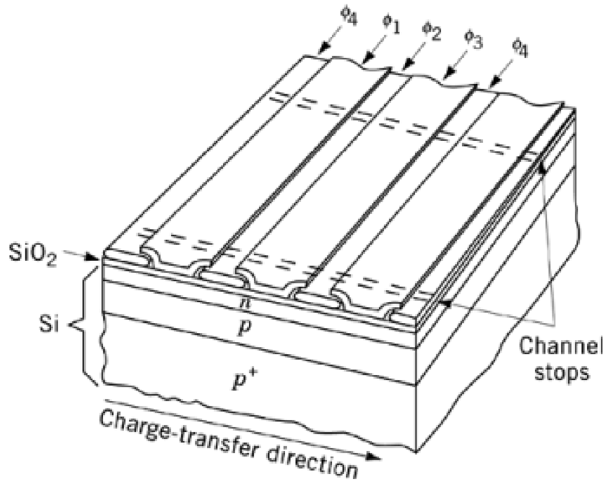

Fig. 11. Cutaway view of a CCD shift register where the φ_i represent gate electrodes. Voltage pulses applied to the phase gates move photogenerated charge in the charge-transfer direction. The channel stops confine the charge during integration and transfer. See text.

metal layer for this purpose. Finally, the CCD is covered with an overcoat of protective material such as SiO_2 or borophosphosilicate glass. This 500–1000-A thick layer serves as a barrier between the environment and the contamination-sensitive CCD.

5.1.3. Device Type vs Application

The application for which the CCD is designed dictates the variants to the process that are utilized to provide the desired performance enhancements. Consider as an example the effect of front-side illumination of the CCD on photon collection efficiency. Applications that require very high photon collection efficiency in the visible blue, extreme uv, or X-ray spectral bands are not well served by front-side illumination of the CCD. A useful CCD variant for such applications is the back-side illuminated CCD. Back-side illuminated CCDs undergo additional processing to remove the underlying $p+$ substrate from the p-type epitaxial layer. As the name implies, photons impinge upon the device from the back side, thereby avoiding the absorption layers of gate electrodes present in front-side illuminated devices. In this manner, the photon collection efficiency of the device can be improved in the blue, uv, and low energy X-ray photon regimes. Substrate removal is accomplished through the use of an etchant with an etch rate that is highly dependent on the concentration of boron dopant found in the silicon. The process of substrate removal is well understood and highly repeatable. However, thinned (to $\sim$25 μm) back-side illuminated CCDs are typically more costly than thick front-side illuminated devices. The additional cost is associated with the reduction of mechanical rigidity produced by the removal of the substrate.

Other CCDs have special processing steps that lower the rate at which surface dark current is generated during the interval in which signal charge is collected. One such device is known as the virtual phase CCD (VPCCD) (68). The VPCCD utilizes a series of implanted dopant layers near the surface of the silicon as a means of removing one of the polysilicon deposition steps required for electrode formation. The implanted layers serve as virtual electrodes that force the surface potential of the silicon in these regions to a constant bias during operation. These virtual electrodes replace two of the four gate phases described in the generic CCD process. The two remaining gate control phases are incorporated into a single physical gate electrode, again by means of ion-implanted layers in the silicon. Thus, the top side of the VPCCD pixel is only partially covered by the polysilicon gate electrode. The ion-implanted layers provide storage capability and unidirectional charge transfer as the single polysilicon electrode phase is clocked. The virtual electrodes also serve to greatly reduce the rate of surface-related dark current generated in the CCD. At 25°C the nominal dark current value of a VPCCD is 0.5 nA/cm^2, which is nearly five times lower than the dark current found in a typical buried channel CCD.

A second device having additional specialized ion-implanted layers is the multipinned phase (MPP) CCD (69). The MPP device is a compromise between a multiphase and a virtual phase CCD, and is becoming the CCD of choice for scientific applications. As in the generic multiphase CCD, the entire charge storage region is covered by polysilicon gates. However, prior to the electrode deposition, additional dopant layers are ion implanted into the silicon. These implanted dopant layers enable the MPP CCD to integrate charge with the applied gate bias set so as to attract opposite polarity charges to the Si–SiO$_2$ interface. This method of operation produces the lowest possible dark currents, rivaling or exceeding the performance of the virtual phase CCD. Operation of the CCD in the MPP mode does, however, reduce the total charge storage capacity to typically 20% of that of an equivalent, non-MPP, device. Although front-side illuminated devices are available, the MPP CCD is typically back-side illuminated in order to achieve state-of-the-art photon collection performance. Even with this stipulation the MPP CCD is still a popular detector due to its availability in various array sizes and formats specifically designed for scientific applications.

5.2. Silicon Photodiodes

The popularity of silicon photodiodes is directly related to the ability to detect photons over a spectral range spanning the near-ir to low energy X-ray regimes. Typical spectral response characteristics are given in Figure 9**a**. The fast response time of < 1 μs is attractive when compared to the response times of photoconductive or bolometer-based devices. The silicon photodiode has a responsivity ~ 0.4 A/W at the peak response wavelength. Some manufacturers list NEP values of $< 2 \times 10^{-15}$ W/Hz$^{1/2}$ and $D*$ above 1×10^{14} cm·Hz$^{1/2}$/W and optical areas of 1–10 mm^2. The photodiode has proven to be a useful tool for photon-counting and imaging applications over the entire range of spectral sensitivity and has been utilized in the visible portion of the spectrum for power generation (70, 71).

Silicon photodiodes are available in both discrete and array formats. The simplicity of the discrete photodiode makes this device one of the least expensive photon detectors available. Discrete photodiodes are merely *p*–*n* homojunctions and are available from numerous manufacturers. Typical commercially available devices have one to four discrete diode detectors per package and frequently device manufacturers include operational amplifier-based readout electronics inside the packaged device for ease of use. Discrete photodiodes can be used in a myriad of applications including high speed optical switching, intensity determination for automatic exposure control circuitry in film cameras, and photon counting for spectroscopic analyses (72).

Photodiode arrays are more complex than their discrete counterparts due to the difficulty of directing the signal information from each diode to off-chip electronics. The more common linear arrays contain internal multiplexing circuitry located on the periphery of the imaging area. This circuitry amplifies and buffers the signal from each diode, presenting the information from each pixel through a single output amplifier in a controlled, time-sequenced fashion. The performance characteristics of linear photodiode arrays typically rival those obtained from discrete diodes. Arrays ranging in size from 1 × 64 pixels up to 1 × 4096 pixels and larger are available from commercial sources. Linear photodiode arrays are commonly found in high resolution image scanning applications such as photocopiers and facsimile (FAX) machines and hand-held scanners (73).

As for linear photodiode arrays, two-dimensional (2D) photodiode arrays require internally integrated circuitry to mediate the signal information from each pixel. However, with the exception of the outermost rows and columns, the pixels in 2D arrays are surrounded on all sides by other pixels. Thus the required circuitry cannot reside solely on the periphery of the array but must be integrated into the actual pixel site. In a 2D array, each pixel consists of both a photodiode and electronic circuitry designed to attach or detach that diode from the readout electronics located at the chip periphery. The voltage pulses that control the time-sequenced readout are generated from two multiplexing circuits, one each for the x- and y-chip dimensions, which are also located at the chip periphery. In its simplest form, the 2D photodiode array utilizes a large capacitor that is common to all pixels in a given row to sequentially convert the signal charge from each pixel to a voltage. The resulting signal voltage is very small, resulting in a signal-to-noise ratio roughly one-half that of an equivalent format CCD array. Generally, device performance varies inversely with the number of pixels in the array. Prior to $\sim$ 1984, 2D photodiode arrays were heavily utilized in commercial imaging applications such as video cameras. Recently, CCDs and metal oxide semiconductor (MOS) arrays, 2D imaging arrays that utilize p–n diodes as photosites, and complimentary metal oxide semiconductor (CMOS)-based components for readout circuitry, have emerged as strong competitors in this arena. Nevertheless some 2D standard video format photodiode arrays are still manufactured. These devices are most useful in situations unsuited for CCD and CMOS-based imagers, such as ionizing radiation environments.

In addition to being a popular image detector, the silicon homojunction photodiode and avalanche photodiode (74) can also be used for power generation by operating the device in the photovoltaic mode. In this mode, incident photons produce a voltage drop across the device that is proportional to the number of absorbed photons. When a finite load resistance is placed across the diode leads, a current is produced. Thus, silicon homojunction diodes can be used to convert optical energy into electrical energy. The energy conversion efficiency for common silicon photocells is in the 3–15% range depending on the specifics of the device design. High levels of illumination are required to produce useful output power. For typical photosensitive cells an illumination of 10 lux can produce an open-circuit output voltage of $\sim$ 0.5 V. However, any desired voltage or current can be generated by the appropriate series or parallel interconnection of multiple individual elements. Whereas silicon photodiodes are not as efficient at power generation as more exotic Group 2–16 (II–VI) and Group 13–15 (III–V) materials, these devices are commonly utilized as power sources for both terrestrial and space-borne applications.

5.2.1. Fabrication

Photodiodes can be made with manufacturing processes resembling those for constructing CMOS as well as bipolar integrated circuits. For a p- on n-diode formation process, the starting wafer is an n-type silicon substrate of roughly 500-μm thickness. The silicon has been doped with either P, As, or Sb during the wafer formation process to a nominal resistivity of $10\ \Omega{\cdot}\mathrm{cm}$. The initial step of the fabrication process consists of growing a thick layer of SiO_2 on the top surface of the silicon wafer through the use of elevated temperatures in a steam and oxygen ambient. Next, circular windows are etched in the SiO_2 layer. The wafer is then placed in a high temperature diffusion furnace which introduces boron dopant into the silicon through the open circular windows. Ion implantation (qv) is a common alternative to high temperature diffusion as a means of boron doping. The result of the doping procedure is the formation of a p– n junction, with one diode formed for every window in the SiO_2. Next, a low resistance material such as aluminum is used to form ohmic contacts to the p-type silicon regions. The aluminum layer is also used to form distinct electrodes, one per diode, to which external connections can be made. Finally, a single common ohmic contact is formed on the back surface of the n-type silicon wafer by an additional metal layer.

The method of diode formation as well as the density and profile of the impurity ions determines the specific optical and electrical performance parameters of the photodiode. When photon absorption occurs in the depletion region of the diode, the resulting carriers are quickly swept from the diode and measured by the readout circuitry. The same behavior occurs for optically induced charge formed within a diffusion length of the depletion region. Charge generated at a distance greater than one diffusion length recombines in the undepleted silicon and consequently cannot be detected as signal charge. A similar fate befalls photogenerated carriers produced in heavily doped or heavily lattice-damaged regions. Heavy surface doping and lattice damage are common by-products of the homojunction formation process. Therefore, the diode fabrication process balances the reduction in the rate of surface dark current generation against the charge collection loss produced by heavily doping the silicon surface. Similarly, the improvement in photon collection efficiency obtained by increasing the thickness of the depletion region must be weighed against the associated increase in bulk-generated dark current.

5.3. CMOS Image Sensors

A relatively new entry in the field of visible photon detection is the CMOS image sensor (75). Sometimes referred to as active pixel sensors (APS), these devices are variants of readout electronics commonly used with ir photodiode arrays (76, 77) that have been modified to allow for the detection of visible photons. Unlike CCD or photodiode imaging arrays, CMOS image sensors have active transistor elements residing in each pixel. These elements are configured into amplification circuitry capable of converting integrated photogenerated charge to a signal voltage inside each pixel. Prior to conversion to a voltage, signal charge is collected and stored in either a diode or MIS capacitor region. Amplifier and multiplexer circuitry residing at the periphery of the imaging area poll, in parallel, each pixel in an image line and transmit the signal voltage measurements to an on-chip analog-to-digital converter (ADC). This readout process continues until every line in the image has been polled and output.

The use of CMOS fabrication technology affords, in theory, a number of advantages over CCD technology. CMOS provides a very high degree of circuit integrability, thereby allowing for complete camera systems to be constructed in a single silicon chip (78). The combination of signal charge detection in the pixel of generation, without the need for transfer through the array, and the use of complementary n- and p-channel field effect transistors (FET) provides for very low power operation. Finally, as CMOS is currently the most popular and most readily available semiconductor process for silicon, imagers can be manufactured at very low cost.

At the time of this writing ($\sim$ 2000), CMOS image sensors are still in their infancy. Compared with CCDs, CMOS imagers suffer from several performance issues, including poor quantum efficiency, fixed pattern noise and image cross talk (79). Quantum efficiency is hampered in two ways. First, the inclusion of active circuitry decreases the photon sensitive area of the pixel, thereby diminishing the total collection area for photons. Second, as compared to a CCD, standard CMOS processes reduce the depth in silicon from which signal charge is collected, thereby retarding the collection efficiency of ca. 600 nm and longer wavelength photons. Fixed pattern noise is introduced into the image through variations in the threshold voltages of interpixel amplifiers across the imaging array, as well as through variations of dark current generation on a pixel-by-pixel basis. Image cross talk occurs through the diffusion of photon charge generated beneath the depletion region of the pixel array. Cross talk also results from changes in pixel operating voltages across the array, which are produced by current flow through the resistance of critical bias lines feeding the pixel circuitry. Much improvement in performance is anticipated over the next few years, and will be required to strenghten the prospects of CMOS imagers for scientific usage.

5.4. Cadmium Sulfide Photoconductor

CdS photoconductive films are prepared by both evaporation of bulk CdS and settling of fine CdS powder from aqueous or organic suspension followed by sintering (80, 81). The evaporated CdS is deposited to a thickness from 100 to 600 nm on ceramic substates. The evaporated films are polycrystalline and are heated to 250°C in oxygen at low pressure to increase photosensitivity. Copper or silver may be diffused into the films to lower the resistivity and reduce contact rectification and noise. The copper acceptor energy level is within 0.1 eV of the valence band edge. Sulfide vacancies produce donor levels and cadmium vacancies produce deep acceptor levels.

The settling technique can be accomplished from an ink that contains 1-μm crystallites of CdS and selected concentrations of $CdCl_2$. The coating is fired in a restricted volume of air at 500–700°C. During the sintering, the $CdCl_2$ acts as a flux and forms a solution with the surface of the grains of the CdS. A few part

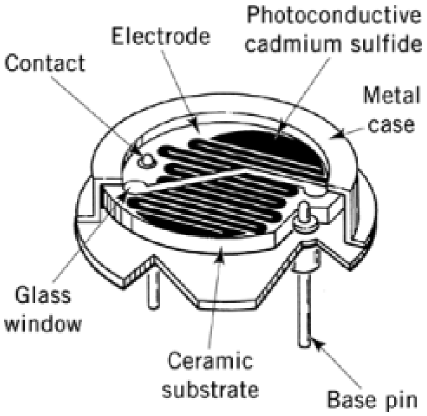

Fig. 12. CdS film detector in a package showing interdigitation to reduce resistance. See text.

per million of chloride and copper (from impurities) enter the crystal lattice and act as activator centers for trapping. Excess chloride evaporates leaving a continuous polycrystalline photoconductive film. The layers are from 5 to 30-μm thick and have a linear I–V relationship.

The films have an area resistance of 100,000–300,000 Ω/square. Most applications, such as switching on outdoor lights at twilight, require a detector resistance of near 1000 Ω to operate the switching circuit without the need of impedance matching electronics. Appropriate impedance is accomplished by depositing the contacts in an interdigitated geometry as shown in Figure 12. A protective film is deposited over the detector and contacts to provide for long-term stability or the detector structure is mounted in a hermetic package as shown. The spectral sensitivity for the thin-film CdS detector is shown in Figure 9**a**. The response shape is similar to that of the human eye (see Table 1).

5.5. GaAsP and InGaAs Photodiodes

Gallium–arsenic (GaAs) and gallium–arsenic–phosphorus (GaAsP) diodes are fabricated as photodiodes as well as light emitters. Fabrication is typically with mesa etch technology of the films of GaAsP or InGaAs grown (82) by the vapor-phase epitaxial process using metal organic chemical vapor deposition (MOCVD). This growth technique results in impurity densities $< 1 \times 10^{14}$ atoms/cm^3. The spectral cutoff range extends from 500 to 900 nm depending on the phosphorus content. These detectors can be used for color discrimination and do not require expensive interference filters. Emitter–diode pairs are utilized for very high impedance signal coupling in high speed integrated circuits. Spectral sensitivity is shown in Figure 9**a** for typical GaAs and GaAsP photodiodes. Surface leakage, caused by the lack of a native surface-passivation technology such as SiO_2 for Si detectors. is the most significant performance limitation for diodes in made from this material system.

The indium–gallium–arsenside, InGaAs, photodiode is becoming a very popular detector for very near ir and short wavelength ir radiation. Making use of improved epitaxial growth techniques, InGaAs devices exist with performance rivalling or surpassing HgCdTe. The available cutoff wavelength of commercially available discrete InGaAs photodiodes extends to 2.5 μm. Linear InGaAs arrays are available with cutoff wavelengths as high as 2.3 μm (see Table 1), enabling such research efforts as room temperature atmospheric spectroscopy (83) and environmental monitoring (84). Uncooled InAsSbP/InGaAs photodiodes with good performance characteristics out to 3.4-μm cutoff wavelength have also been reported (85).

5.6. PbS and PbSe Photoconductors

The lead chalcogenides, PbS, PbSe, and PbTe, were among the first ir-detector materials to have been investigated. Although photovoltaic effects are observed with *p–n* junctions in single-crystal material the response is quite poor and not reproducible. However, very sensitive photoconductors are prepared as polycrystalline thin films, ~ 1-μm thick, which are deposited on glass (qv) or quartz substrates between gold or graphite electrodes.

Detector elements are prepared either by sublimation in the presence of a small partial pressure of O_2 or by chemical deposition from alkaline solution containing a lead salt and thiourea or selenourea (86). Lead sulfide and lead selenide deposit from solutions as mirror-like coatings made up of cubic crystallites 0.2–1 μm on a side. The reaction may nominally be represented by the following:

$$Pb^{2+} + SC(NH_2)_2 + 2\ OH^- \longrightarrow PbS + C({=}NH)_2 + 2\ H_2O$$

The actual reaction probably is more complex. The photoconductive behavior depends on the pH of the solution from which deposition occurs. It is likely that oxygen-containing compounds are present in the deposited films. For either method of preparation, the effect of oxygen, which is introduced during preparation or by subsequent heat treatment in air or oxygen, is critical for the development of optimum sensitivity. Maximum sensitivity is obtained near the point at which the film conductivity type changes from *n* to *p*. The long response times are suggestive of trapping. It is likely that deep trapping states are located at the oxidized surface of the micrograins (87, 88). The evaporation technique produces the best results especially for PbSe and the more obsolete PbTe. The spectral sensitivity is shown in Figure 9**b** for different operating temperatures (see Table 1).

5.7. Platinum Silicide Schottky Barrier Arrays

The Pt:Si detector (89–91) essentially is a metal semiconductor barrier whereby the platinum silicide is a quasimetal that generates a small energy barrier to electrons. The effective photons are absorbed in a very thin region of the silicide next to the barrier and generate free electrons that flow over the barrier and tunnel through it into the *n*-type silicon. The efficiency of this process is only a few percent even at high energies (short wavelengths) because of the low electron diffusion coefficient in the silicide. At wavelengths beyond 1 μm, the efficiency drops off dramatically because of decreasing tunneling probability for the lower energy electrons. The effective quantum efficiency is ~ 0.1% at 4.8-μm wavelength.

Techniques of platinum deposition vary but sputtering and annealing of a very thin layer of platinum produces a uniform platinum silicide film with < 0.3% variation in responsivity in an area of 2×2 cm. Details of deposition and annealing processes are considered trade secrets by the manufacturers. Deposition is typically onto silicon integrated circuit (IC) chips having a readout structure. Small regions of the IC chip at each pixel are dedicated for the silicide detector element. The readout is typically an in-line charge-coupled device. The spectral sensitivity is shown in Figure 9**b** and array information is given in Table 1.

Although the photon efficiency is quite low, focal plane performance for ir imaging of ambient temperature scenes is acceptable because of long television display frame time, reasonably low detector noise, and the excellent uniformity of responsivity which allows for high on-chip input gain without offset correction. The responsivity is ~ 10 mV degree delta scene temperature using *f*/2 optics and scene sensitivity with large arrays is ~ 0.1°C. The Pt:Si detector finds typical use in security and defense-related applications, but is also useful in spectroscopy (92) and other applications where device cooling is not a significant systems issue.

5.8. InSb Photodiode Detectors and Arrays

Sensitive photodiodes (93, 94) have been fabricated from single-crystal InSb using cadmium or zinc to form a *p*-type region in bulk *n*-type material. High quality InSb crystals can be grown by the infinite-melt process

(95, 96) where an InSb film is grown epitaxially (from the liquid phase) on a slice of InSb that was prepared in a conventional Czochralski vertical puller. The diode formation process typically is a closed-tube diffusion. Cleaned and etched samples of InSb are placed in a quartz ampul with a limited amount of zinc or cadmium. After evacuation and sealing, the ampul is heated to $\sim$ 50°C below the crystal melting point. The metal vaporizes partially or completely, depending on the amount, volume of ampul, and temperature, and diffuses into the crystal after a few hours. The impurity–diffusion profile approximates the error–function law and the p–n junction is 1–5 μm below the surface. Diode arrays (16) are formed by etching mesas $\sim$ 50 μm square. Typical performance of InSb detectors is given in Table 1 and the spectral sensitivity is shown in Figure 9**c**. Up to 480×640 matrix arrays of InSb photodiodes in a mesa configuration have been demonstrated. Commercial units of 256×256 are available. The mesa detector array is mated to a silicon chip having an array of amplifiers and multiplex circuitry. Each diode is connected to an amplifier input. The hybridization process consists of forming indium bumps on each diode mesa and on each amplifier input, using a photolithographic process and In evaporation and pressing the detector array chip to the silicon integrated circuit chip. The ir radiation must pass through the InSb chip to reach the photodiode junction. To improve quantum efficiency the InSb is grown on GaAs or GaAsSb substrates as a thin layer. Quantum efficiency is $>$ 50% for wavelengths $>$ 2 μm and less than the cutoff of InSb, 5.3 μm. A protective coating (passivation) of the InSb photodiode for stable operation over several hours without frequent signal normalizations has not been found. However, ir imaging cameras using hybrid InSb focal planes are a commercial reality. In a real-time imaging configuration the scene sensitivity is $\sim$ 0.04°C using an InSb ir camera. As a result of their commercial availability, InSb arrays are finding increased use in infrared astronomy (97) and other scientific applications.

5.9. Mercury Cadmium Telluride

HgCdTe has proven to be an excellent ir detector material (2) where the CdTe content can be readily adjusted to obtain cutoff wavelengths from 2 to 20 μm. The benefit is high spectral sensitivity of the photon detector, low defect density, and high cooling efficiency. The dependence of energy gap on mole fraction is linear. For $\mathrm{Hg}_{1--x}\mathrm{Cd}_x\mathrm{Te}$, the x values of most interest lie between 0.17 and 0.50. The need for large focal planes up to 2×2 cm has dramatically changed the direction of single-crystal HgCdTe growth technology.

5.9.1. Crystal Growth

The method of solid-state recrystallization (quench and anneal) was marginally adequate during the 1970s and 1980s for linear photoconductor arrays used in military night vision systems, but the quenching kinetics restricted sample size to $6\,\mathrm{mm} \times 2\,\mathrm{cm}$. The crystals had many low angle grain boundaries, defect densities were high, and there were large nonuniformities in composition and carrier concentration. Therefore epitaxial growth technologies were developed. Crystal growers were hampered, however, by the lack of suitable substrate material until methods were developed to grow the HgCdTe films onto large-area silicon and GaAs single crystals. The problem with misfit dislocations has not as of this writing ($\sim$ 2000) been satisfactorily solved except for detector cutoff wavelengths $<$ 5 μm. Thus, CdTe single crystals are used to obtain large, low defect density substrates for growth from the liquid phase. Lattice matching is achieved by adding 3% Zn by atomic weight.

Large-area CdZnTe substrates form the basis for liquid-phase epitaxy (LPE) growth of mid- and long wavelength ir HgCdTe detector material. Substrates are obtained from 3.5-kg CdZnTe ingots grown in graphite boats in sealed quartz ampuls (98). The horizontal Bridgman growth process yields $41 \times 6.4 \times 5.0$ cm semi-cylindrical ingots having large single-crystal portions that are then sectioned, sawed into slabs, and diced into required dimensions. The substrate surfaces are diamond turned and etched to assure flat, damage-free surfaces. Standard substrate sizes are 3.6×2.0 cm and 3.6×1.5 cm, but the ability to obtain single-crystal $< 111 >$ oriented CdTe substrates, as large as 5.1×7.6 cm, has already been demonstrated. The material

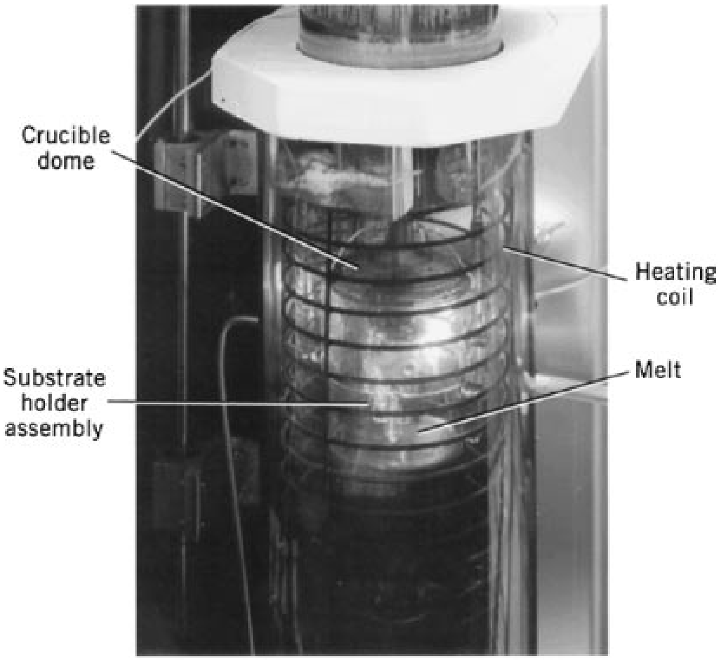

Fig. 13. Furnace reactor for the growth of HgCdTe films on CdZnTe substrates using the liquid-phase epitaxial process. The melt is tellurium in a quartz crucible. A mercury reservoir in a cooler zone maintains the required Hg over-pressure.

typically exhibits dislocation densities of $1 \times 10^5/\text{cm}^2$ and high purity as judged by Hall measurement made on evaluation samples of n-type LPE films grown on these substrates.

Liquid-phase epitaxial films (98, 99) are grown in production prototype dipping reactors as shown in Figure 13 using the CdZnTe substrates. Film growth is both from tellurium and mercury solutions. Phase diagrams for the Te and Hg corners are shown in Figure 14. Growth is from lightly (ca $5 \times 10^{14}/\text{cm}^3$) indium-doped 4000-g tellurium solutions. The mercury vapor pressure is maintained by a mercury reservoir positioned in an independently controlled furnace zone. Up to 54 cm^2 of material can be grown from the largest reactors in a single run. Multiple furnace zones in the vicinity of the melt crucible permit adjustment of the melt temperature profile. The substrates are positioned horizontally during growth and rotated to promote uniformity of composition. The holder design allows substrates to be reoriented vertically for withdrawal, to facilitate melt drainage. LPE films are also grown in mercury solutions of several kilograms in which small amounts of tellurium and cadmium have been added. In both cases, the cutoff wavelength varies $< 0.1\ \mu$m across the entire film.

The films grown in tellurium are annealed in Hg vapor. Mercury atoms diffuse into the films to reduce the density of Hg vacancies that act as acceptor sites. The carrier concentration is shown as a function of anneal temperature in Figure 15. For photoconductive detectors the films are annealed such that the indium donor density is dominant resulting in n-type material having a $1 \times 10^{15}/\text{cm}^3$ excess electron density. Minority carrier lifetime is typically 1–5 μs at 77 K. For photodiodes the films are annealed to an acceptor (via Hg vacancies) density of $3 \times 10^{16}/\text{cm}^3$. Carrier lifetimes are < 50 ns at 77 K. Extrinsic acceptor doping is being developed to replace vacancy doping to achieve longer minority carrier lifetime and lower dark current density. Film thickness is 40–80 μm.

Films grown in Hg (99, 100) are usually structured to make heterojunction photodiode arrays. The first or base layer is narrower band gap HgCdTe, grown on CdZnTe substrates, doped with indium for excess electrons

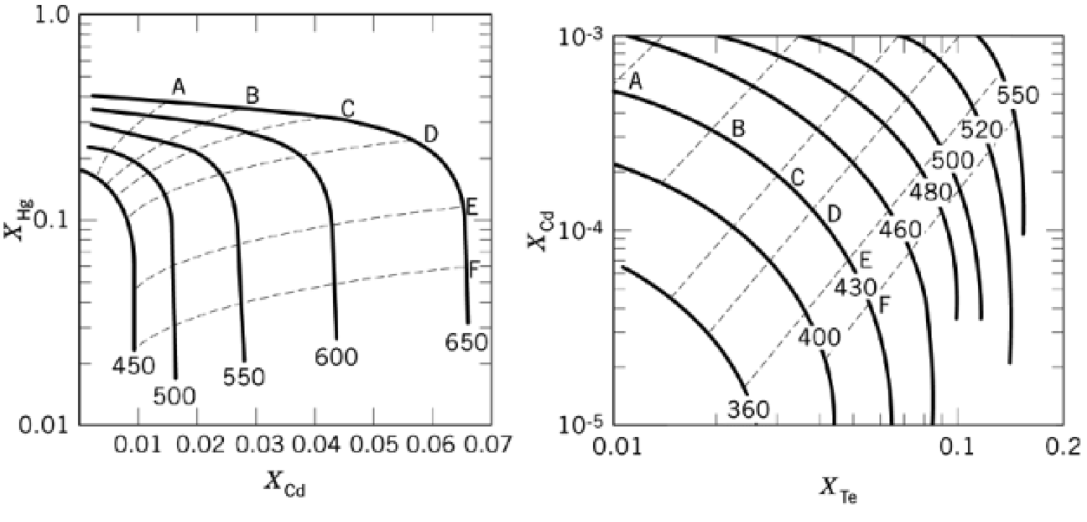

(a) (b)

Fig. 14. Phase diagrams of HgCdTe used to define the liquid-phase epitaxial growth process where composition is in mole fraction, X, and the numbers represent temperatures in °C: (**a**) Te-rich corner where the dotted lines A–F correspond to values of X_{Te} of 0.1, 0.2, 0.3, 0.5, 0.8, and 0.9, respectively, and (**b**) Hg-rich corner where A–F correspond to values of X_{Hg} of 0.9, 0.8, 0.6, 0.4, 0.2, and 0.1, respectively.

(n-type) in the $3 \times 10^{16}/\mathrm{cm}^3$ range and is 10-μm thick. The second or cap layer is wider band gap HgCdTe, doped with arsenic for excess holes (p-type) in the $5 \times 10^{15}/\mathrm{cm}^3$ range and is 4-μm thick. The composite HgCdTe film is photolithographically etched part way into the base layer to form an array of mesas, each one being a photodiode detector element. The p–n junction is close to or coincident with the metallurgical heterojunction. For infrared detection in the 8–12 μm atmospheric spectral window the base layer CdTe content is $\sim$ 20% and the cap layer CdTe content is $\sim$ 30%.

5.9.2. Photoconductive Detectors Arrays

Greater than 50,000 HgCdTe linear arrays (101, 102) have been produced in the United States since 1972 for the Department of Defense IR systems ranging from night vision for M1 tanks to targeting sights for smart weapons. These common module detector arrays consist of 180 elements photoetched on a 50-μm pitch. Virtually all of the material used for these arrays was prepared by the solid-state recrystallization process. Small slabs of material were epoxied to sapphire or ceramic and were thinned to 8 μm. The newer epitaxial HgCdTe is also epoxied to the ceramic with the film side down. The material is thinned by diamond turning and the CdZnTe substrate is removed. In each case an 8-μm thick layer of HgCdTe remains. The last few micrometers of removed HgCdTe must be carefully etched to avoid generating defects. The arrays are defined by photoetching, passivated using a ZnS film, and indium electrical contacts are applied. The contacts define the optically active area of $\sim 2 \times 10^{-5}$ cm^2. The arrays are mounted in a vacuum Dewar for cryogenic cooling. Each element is connected to a series resistance bias circuit and a-c coupled to an amplifier. Detector resistance is nominally 100 Ω and bias current is $\sim$ 2 mA. The signal voltage is given by equation 13 and the responsivity by equation 34.

$$R_V = \eta\tau V/h\nu n v \qquad (34)$$

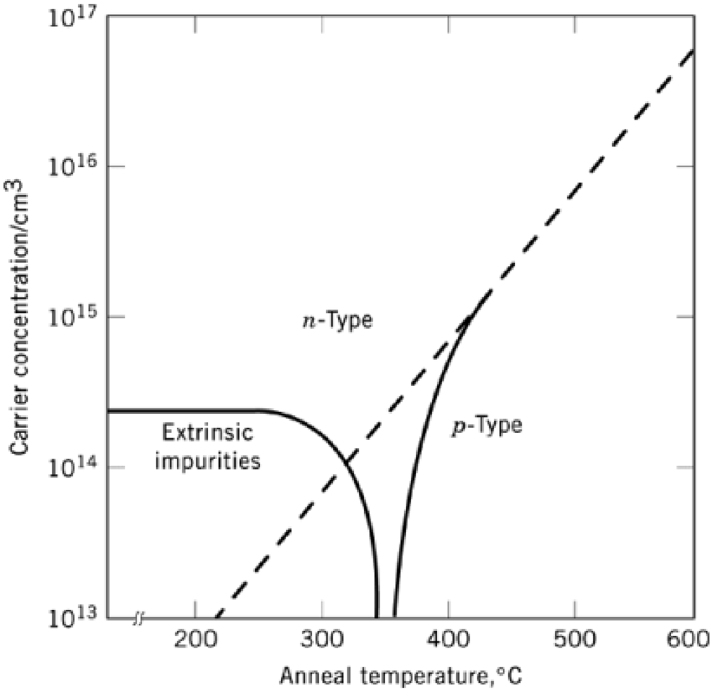

Fig. 15. Excess carrier concentration in HgCdTe in a saturated Hg vapor as a function of temperature where the dashed line represents Hg vacancies. The extrinsic impurity concentration can be adjusted in the growth process from low 10^{14} up to mid-10^{17}. Low temperature annealing reduces Hg vacancy concentration and acceptor density.

The responsivity becomes independent of the bias voltage, V, when the electric field-induced sweep time of the holes equals the hole lifetime.

For a well-designed, well-made HgCdTe photoconductor detector (103, 104), g-r noise is dominant and may be expressed in terms of a minority carrier density p and majority carrier density n. Semiconductor noise analysis for the HgCdTe photoconductor yields,

$$V_{\mathrm{g-r}}^2 = \frac{4p\tau V^2 \Delta f}{n(n+p)v} \qquad (35)$$

The responsivity and g-r noise may be analyzed to obtain background photon flux and temperature dependence of responsivity, noise, and detectivity. Typically, $n > p$, and both are determined by shallow impurity levels. The minority carrier density is the sum of thermal and optical contributions,

$$p = \frac{n_i^2}{n} + \frac{\eta\phi_B\tau}{t} \qquad (36)$$

where, typically, the background flux φ_B is much greater than the signal flux φ_s. The lifetime, τ, is $\sim 1\ \mu$s but for narrow band gap defect-free detectors it becomes the Auger lifetime and can be calculated readily from basic semiconductor properties (101). The cooling requirement is determined according to equation 36 because n_{i} is an exponential function of band gap energy and temperature. Combining equations 35 and 36 detectivity can be expressed as follows:

$$D_\lambda^* = \frac{\eta}{2h\nu}\left(\frac{\tau}{pt}\right)^{1/2} \qquad (37)$$

At low background flux this gives the temperature dependence of the $D_\lambda{}^*$ shown in Figure 4. At high flux, the $D_\lambda{}^*$ (eq. 37) reduces to equation 12 except for a factor of $(2)^{1/2}$, which is a result of the random recombination process not present in diodes. The scene sensitivity of a scanning photoconductor array ir camera is $\sim 0.15°$C.

The long minority carrier lifetime in n-type HgCdTe has been exploited to perform signal processing in the element (SPRITE) (105). The bias field is adjusted to sweep the photogenerated holes along the HgCdTe detector element synchronously with the scanned image creating a time delay and integration (TDI) enhancement of the signal-to-noise ratio.

5.9.3. Photovoltaic Detectors, Arrays, and Focal Planes

The two popular types of photodiode arrays in HgCdTe are based on homojunction (106) and heterojunction (107, 108) technologies. Homojunction diode arrays are fabricated with p-type epitaxial HgCdTe. The surface of the grown HgCdTe film is flattened by diamond milling and chemical lapping using a weak solution of bromine in methanol. The epitaxial film is then epoxied to a silicon chip having an array of amplifiers (typically on 50-μm centers) and readout multiplexer (mux) circuitry. The CdZnTe substrate is milled away and the HgCdTe is thinned to $\sim$ 10 μm. An array of small (10–20 μm) holes is etched in the HgCdTe film such that each hole is located over an amplifier input pad of the silicon IC chip. The diodes are made by implanting boron (150 kV, $1 \times 14/\mathrm{cm}^2$) through a 500-nm ZnS layer. Planar diodes are generated using a patterned photoresist to define the implanted regions located between the holes. The implant process disrupts the lattice, creating Hg ion interstitials that cause the formation of very shallow donor states. The damage layer extends $\sim$ 150 nm from the surface and the n–p junction varies from 2 to 8-μm deep depending on the implant and annealing conditions. The fabrication is completed by applying a CdTe passivation layer ($\sim$ 1-μm thick) directly to the HgCdTe surface, forming a ZnS layer for antireflection and electrical isolation and formation of a metal film lead to connect each implanted n region to each amplifier input. Infrared illumination is directed onto the HgCdTe film and quantum efficiency typically exceeds 75%. Because ir focal planes are typically cooled to below 100 K the differential coefficient of thermal expansion causes the shrinking silicon to put tensile stress on the HgCdTe film. However, the thinness of the film and the presence of the holes allow the HgCdTe to strain retaining the integrity of the epoxy film and the electrical contacts. Array dimensions up to 2.5 cm have proven reliable.

Heterojunction diode arrays utilize the grown p–n junction and mesa etch technology. The mesa arrays are passivated by a thin layer ($\sim$ 500 nm) of CdTe using an evaporation or molecular beam epitaxial process. Annealing at 250°C in a Hg atmosphere creates a short ($\sim$ 100 nm) graded layer from the CdTe to the HgCdTe. The benefit of CdTe passivation is efficient isolation of the p–n junction from the surface, low dark current noise, and immunity to ionization radiation. As for the InSb hybrid arrays, indium bumps are formed using evaporation at the center of each mesa and on each amplifier contact pad of the silicon integrated circuit chip. The two chips are pressed together in a bump bonding process called hybridization (109). Sometimes the space between the chips is filled with epoxy. Infrared illumination is through the CdZnTe substrate that has been coated with ZnS for antireflection. Quantum efficiency typically exceeds 75%.

HgCdTe photodiode performance for the most part depends on high quantum efficiency and low dark current density (110, 111) as expressed by equations 23 and 25. Typical values of R_0A at 77 K are shown as a function of cutoff wavelength in Figure 16 (95). HgCdTe diodes sensitive out to a wavelength of 10.5 μm have shown ideal diffusion current limitation down to 50 K. Values of R_0A have exceeded $1 \times 10^6\ \Omega{\cdot}\mathrm{cm}^2$. Spectral sensitivities for three compositions of HgCdTe detectors are shown in Figure 9**a** and 9**c**. More information is listed in Table 1. The scene sensitivity with a HgCdTe diode area array cooled to 80 K is $\sim 0.02°$C for ambient temperature scenes.

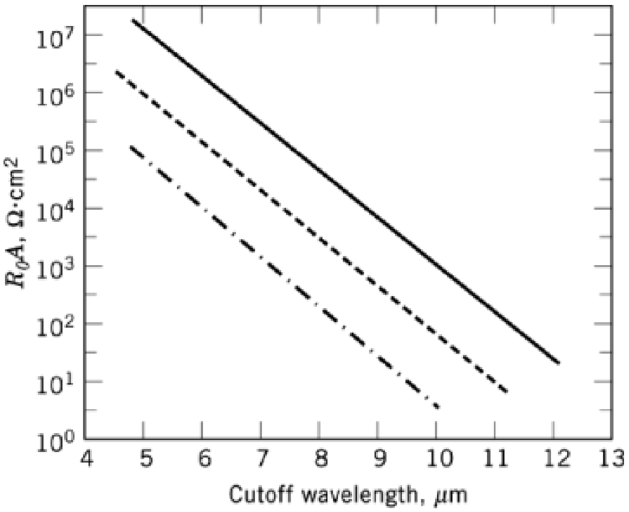

Fig. 16. Resistance area (R_0A) product for HgCdTe photodiodes cooled to 77 K. The solid line represents the theoretical limit, the dashed lines (— —) and (— • —) high and low performance, respectively. Dark current caused by defects lowers R_0A and detector sensitivity. In the high performance range dark current is an exponential function of cutoff wavelength and temperature.

5.10. Doped Germanium and Silicon Photoconductors

The extrinsic photoconductors are typically single-crystal germanium doped with zinc, cadmium, mercury, boron, and gold (112, 113) and silicon doped with indium, gallium, or arsenic (114). The doping density ranges from 1×10^{15} to 1×10^{17} impurity atoms/cm^3 leading, respectively, from low ($1\ \text{cm}^{-1}$) to higher absorption coefficient ($50\ \text{cm}^{-1}$).

Information on ionization energies, solubilities, diffusion coefficients, and solid–liquid distribution coefficients is available for many impurities from nearly all columns of the Periodic Table (113). Extrinsic Ge and Si have been used almost exclusively for ir detector applications. Of the impurities, Cu, Au, Zn, Cd, Hg, and some of the elements of Groups 13 (III) and 15 (V) have been used in detectors. Germanium and silicon, which are used in the preparation of detectors, must be of high purity before they are doped with the desired activator impurity in order to avoid unwanted compensation by impurities with smaller ionization energies than the activator. The required purity can be achieved by zone refining in which a short molten zone is repeatedly passed from end to end of an ingot of impure Ge or Si. Impurities having distribution coefficients larger than unity collect near the seed. The concentration of electrically active residual impurities in the center portion of the ingot can be reduced to 10^{12}–10^{13}/cm^3. Single crystals can be grown using the Czochralski method, in which an oriented seed crystal is brought into contact with the melt and then is withdrawn slowly while being rotated, or using a horizontal zone melting method, in which a seed crystal is melted onto one end of a polycrystalline ingot. A molten zone is produced at the junction of the ingot and seed and is moved slowly along the ingot, leaving behind a single crystal. All of these operations must be carried out in an inert or reducing atmosphere in order to prevent oxidation of the germanium or silicon.

In most cases, the activator impurity must be incorporated during crystal growth. An appropriate amount of impurity element is dissolved in the molten Ge and, as crystal growth proceeds, enters the crystal at a concentration that depends on the magnitude of the distribution coefficient. For volatile impurities, eg, Zn, Cd, and Hg, special precautions must be taken to maintain a constant impurity concentration in the melt. Growth occurs either in a sealed tube to prevent escape of the impurity vapor or in a flow system in which loss caused by vaporization from the melt is replenished from an upstream reservoir.

Some impurities, eg, Cu, Ag, Ni, Co, and Fe in Ge, and In, Ga, and As in Si, have diffusion coefficients that are large enough to permit doping by solid-state diffusion at well below the melting point of the host crystal. A thin layer of the diffusant, which is deposited on the surface of the crystal by electroplating, vacuum evaporation, or electrochemical replacement, serves as the source for diffusion. After homogeneity is achieved, the sample is quenched. The alloyed surface layer must be removed by lapping and etching before the electrical contacts are applied. The impurity concentration should be as large as possible, within limits, in order to maximize the absorption coefficient. In some cases, the concentration is limited by the impurity solubility, which may be small depending on the element. For impurities of high solubilities, the upper limit is set by the onset of impurity banding. When the average separation of impurity atoms in the lattice is small enough, conduction by direct transfer of carriers from atom to atom can occur. Impurity banding limits the extent by which cooling can reduce the dark current and, therefore, the noise, in Ge and Si. This finding is significant above impurity concentrations of $\sim 10^{16}/\text{cm}^3$.

Impurities other than those from Groups 13 (III) and 15 (V) generally exhibit two or more impurity levels in Ge. If an activator that is not of the lowest lying level is used, the lower lying levels must be compensated for by addition of an impurity of the opposite conductivity type. For example, if the second Zn acceptor level for 0.095 eV is to be used, the lower lying level at 0.035 eV must be compensated for by addition of a donor impurity, eg, As, in a concentration slightly greater than that of Zn. Electrons from the As donors fall into the low lying Zn level and render it inactive. A special case is the lowest lying Au level; Au acts as a donor at 0.045 eV above the valence band. If a shallow acceptor, eg, Ga, is added in a concentration that is slightly less than that of Au, electrons from the donor level fall into the Ga level. At low temperatures, holes that are bound to the compensated Au centers can be photoexcited to yield photoconductivity with a long wavelength threshold at $\sim 25\ \mu$m. Single-detector elements and arrays are formed by dicing and etching and attachment of electrical contacts. Linear arrays of several hundred elements have been made. The spectral sensitivities of doped Si and Ge detectors are shown in Figure 9**c** and 9**d**. See Table 1 for other information. Monolithic and hybrid extrinsic focal planes have also been demonstrated (115, 116). Such arrays play an important role in areas requiring detection of very long wavelength ir radiation, and are capable of observing at the sensitivity limits imposed by natural sky background radiation (117).

5.11. GaAs–AlGaAs Quantum Well Arrays

The quantum well ir detector (118–120) is a technology based on the artificial structure called a superlattice. Infrared detection out to 15-μm wavelength and beyond has been achieved using engineered material having a controlled energy gap. The technique utilizes multiple stacked layers of semiconducting material, each having a tailored band gap energy, such that a series of potential wells exists in the direction normal to the layers. Typically, very thin layers of GaAs and AlGaAs are grown by molecular beam epitaxy (MBE). The MBE process is conducted in stainless tubing and is simply controlled evaporation of the elements from side chambers into a main chamber containing a wafer of the substrate material, typically GaAs. The electron wave function is confined in the potential wells when the photon-generated electron wavelength is nominally the layer thickness ($\sim$ 10 nm). The electrons are freed from the wells by photons and a signal is detected with the application of an external bias voltage.

AlGaAs QWIP focal planes have achieved sufficient sensitivity out to 10-μm wavelength to result in scene temperature sensitivity of $\sim 0.04^\circ$C when the focal plane is cooled to 70 K (121). Spectral sensitivity is shown in Figure 9**c** and array information is given in Table 1. To date, QWIP devices have been utilized in a number of scientific applications, including geology (122), medicine (120), and astronomy (123), as well as in public service applications such as fire fighting.

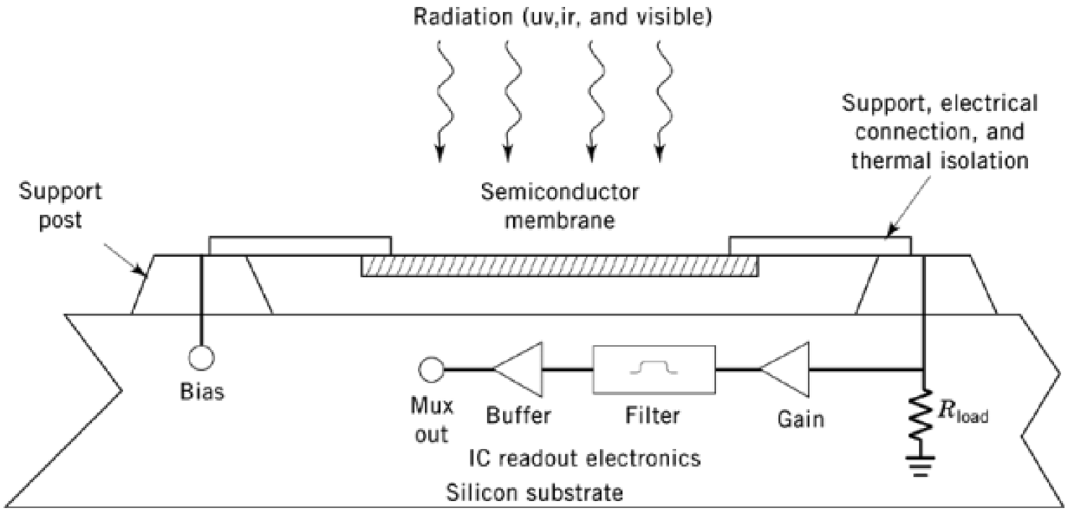

Fig. 17. Cross-sectional schematic of a microbolometer photodetector. Micromachining is used to construct small, very low mass detectors. The dimension of a detector–amplifier cell is 50 μm. Mux=multiplexer, IC=integrated circuit.

5.12. Semiconductor Bolometer Arrays

The use of bolometers to sense ir radiation is not new. What is different is that, rather than having a single cell of large dimension, a matrix of miniature cells or microbolometers is created. Rather than a single amplifier connected externally, a custom integrated circuit is built under each cell to form a totally integrated focal plane array as indicated in Figure 17. Key elements of the structure (124, 125) are the thin (100 nm) amorphous silicon (α:Si) or vanadium oxide (VO) thermally sensitive membrane, the thermally insulating support arms, and the integrated circuit underlying this structure. Infrared energy focused on the individual pixels heats the membrane as given by equation 24. The support arms act as electrical contacts but are sufficiently thin and narrow to prevent significant conduction of thermal energy from the membrane to the surroundings. Temperature-dependent electrical resistance of the semiconductor film is monitored by the circuitry and converted into an electrical signal proportional to the incident radiance. This signal is displayed on a standard television monitor, thus forming the image of the scene.

Two technological advances have occurred that make such a structure feasible to build. The first is the development of microetching techniques that can be used to form microscopic structures in silicon and its coatings. This advance makes formation of the membrane and support arms possible with thickness control in the 10-nm range. Cell dimensions of $< 50\ \mu$m have been demonstrated. Scanning electron microscope photos are shown in Figure 18 of an array and a test pixel. The second critical factor is the increased circuit density in silicon integrated circuits, making it possible to build a small circuit for each cell of the array. By doing this, the noise bandwidth of each cell can be minimized, thereby maximizing performance. This device is a thermal detector in the ir and is therefore independent of wavelength. Measured responsivity is $\sim 5 \times 10^5$ V/W and NEP is ~ 50 pW. The focal plane operates at ambient temperature. Imaging arrays having scene sensitivity better than 0.1°C have been demonstrated (see Table 1).

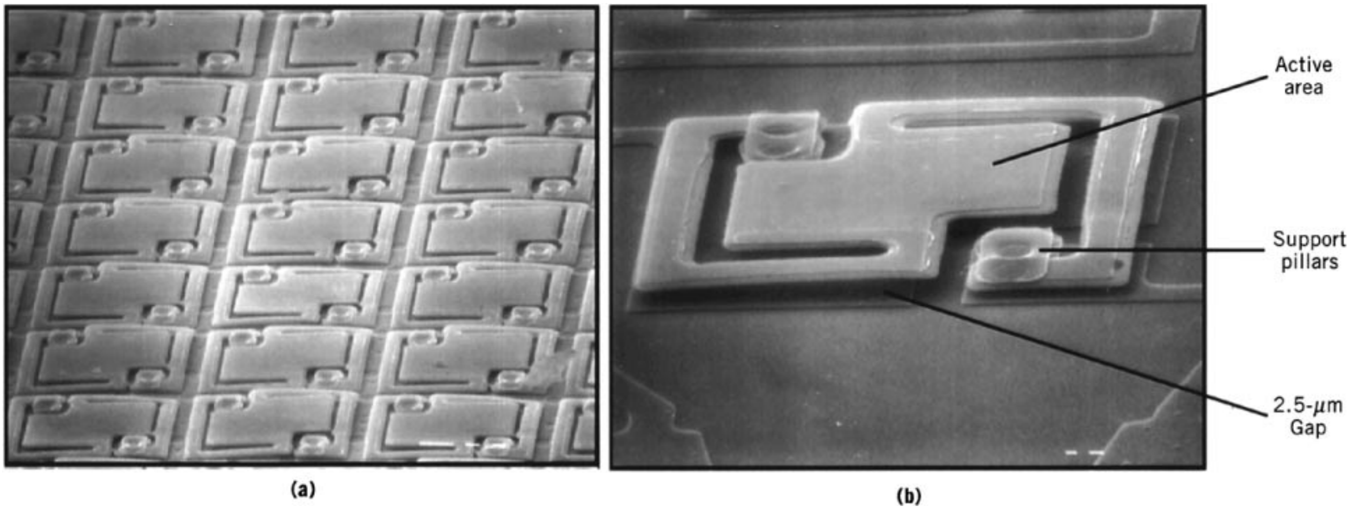

Fig. 18. Microbolometer (**a**) array portion showing pixels on a 50-μm pitch. Each pixel is connected to a readout amplifier in the supporting silicon IC chip. (**b**) Detector having a $35\times40\ \mu\text{m}$ active area. The serpentine arms give excellent thermal isolation and the low mass results in a 10-ms response time, ideal for thermal imaging.

6. Health and Safety Factors

The completed photodetector usually is packaged hermetically in inert glasses or plastics or is enclosed in an evacuated metal or glass container. Although most detector materials are toxic, the means taken to passivate and isolate these materials are often adequate to protect the user. However, there are exceptions. The preparation of detector materials and detector fabrication can present considerable hazards. Some crystal preparation techniques require the use of a toxic substance, eg, Hg, at vapor pressures $>$ 1 MPa (10 atm). Ampul explosions do occur. The electrical circuitry required to operate photodetectors almost always couples to detector devices at low voltages, eg, <10 V; therefore, electrical hazards are minimal. Detectors that are operated at low temperatures are mounted in evacuated containers or Dewars that are partially or nearly completely made of glass. These containers are subject to implosion by improper handling.

BIBLIOGRAPHY

"Photoelectric Cells" in *ECT* 1st ed., Vol. 10, pp. 519–542, by V. K. Zworykin and E. G. Ramberg, Radio Corp. of America; "Phototubes and Photocells" in *ECT* 2nd ed., Vol. 15, pp. 396–443, by C. P. Hadley and co-workers, Radio Corp. of America; "Photodetectors" in *ECT* 3rd ed., Vol. 17, pp. 560–611, by S. R. Borrello, Texas Instruments; "Photodetectors" in *ECT* 4th ed., vol. 18, pp. 861–905, by Sebastiam R. Borrello and Mark V. Wadsworth, Texas Instruments; "Photodetectors" in *ECT* (online), posting date: December 4, 2000.

Cited Publications

1. R. A. Smith, F. E. Jones, and R. P. Chasmar, *The Detection and Measurement of Infrared Radiation*, Oxford University Press, London, 1968.
2. W. L. Wolfe and G. J. Zissis, eds., *The Infrared Handbook*, Rev. ed., Environmental Research Institute of Michigan, Ann Arbor, 1985.

3. P. W. Kruse, L. D. McGlauchlin, and R. B. McQuistan, *Elements of Infrared Technology*, John Wiley & Sons, Inc., New York, 1962.
4. S. M. Ryvkin, *Photoelectric Effects in Semiconductors*, Consultants Bureau, New York, 1964.
5. P. W. Kruse, "The Photon Detection Process", in R. J. Keyes, ed., *Topics in Applied Physics, Optical and Infrared Detectors*, Springer-Verlag, New York, 1980.
6. S. M. Sze, *Physics of Semiconductors*, Wiley-Interscience, New York, 1969.
7. R. D. Hudson, Jr., *Infrared System Engineering*, Wiley-Interscience, New York, 1969.
8. J. A. Jamieson, R. H. McFee, G. N. Plass, R. H. Grube, and R. G. Richards, *Infrared Physics and Engineering*, McGraw-Hill Book Co., Inc., New York, 1963.
9. H. L. Hackforth, *Infrared Radiation*, McGraw-Hill Book Co., New York, 1960.
10. C. S. Williams and O. A. Becklund, *Optics, A Short Course for Engineers and Scientists*, Wiley-Interscience, New York, 1972.
11. M. J. Buckingham, *Noise in Electronic Devices and Systems*, Halsted Press, New York, 1983.
12. S. Borrello and Z. Celik-Butler, *Solid State Electron.* **36**, 407 (1993).
13. R. S. List, *J. Electron.* **22**(8), 1017 (1992).
14. S. R. Borrello, C. G. Roberts, B. H. Breazeale, and G. R. Pruett, *Infrared Phys.* **11**, 225 (1971).
15. C. Hilsum, "Device Physics", in T. S. Moss, ed., *Handbook on Semiconductors*, Vol. 4, North-Holland, New York, 1981.
16. J. H. Longo, D. T. Cheung, A. M. Andrews, C. C. Wang, and J. M. Tracy, *IEEE ED* **25**(2), 213–232 (1978).
17. D. Long, "Photovoltaic and Photoconductive Infrared Detectors", in Ref. 5.
18. M. A. Kinch and S. R. Borrello, *Infrared Phys.* **15**, 111 (1975).
19. L. J. M. Lesser and F. L. J. Sangster, "Charge Transfer Devices", in Ref. 15.
20. F. Milton, "Charge Transfer Devices for Infrared Imaging", in Ref. 5.
21. E. H. Nicollian and J. R. Brews, *MOS Physics and Technology*, John Wiley & Sons, Inc., New York, 1982, Chapt. 2.
22. C. Y. Wei and co-workers, *IEEE Trans. Electron Dev.* **ED-27**(1), 170 (1970).
23. E. H. Putley, "Thermal Detectors", in Ref. 5.
24. A. Rogalski, "Selected Papers on Semiconductor Infrared Devices", in J. Thompson, ed., *SPIE Milestone Series*, SPIE Optical Engineering Press, Bellingham, Wash., 1992.
25. W. D. Rogatto, "Electro-Optics Components", in J. S. Accetta and D. L. Shumaker, eds., *The Infrared & Electro-Optical Systems Handbook*, Vol. 3, SPIE Optical Engineering Press, Bellingham, Wash., 1993.
26. W. S. Boyle and G. E. Smith, *BSTJ Briefs* **49**(4), 587 (1970).
27. G. F. Amelio, M. F. Tompsett, and G. E. Smith, *BSTJ Briefs* **49**(4), 593 (1970).
28. J. R. Janesick and co-workers, *Proc. SPIE* **501**, 2 (1984).
29. J. Hynecek, *IEEE Trans. Electron. Devices* **ED-32**(8), 1421 (1985).
30. K. A. Parulski, *IEEE Trans. Electron. Devices* **ED-32**(8), 1381 (1985).
31. Y. Takemura and co-workers, *IEEE Trans. Electron. Devices* **ED-32**(8), 1402 (1985).
32. D. F. Barbe, *Proc. IEEE* **63**, 38 (1975).
33. D. E. Groom and co-workers, *Nucl. Instr. Meth. Phys. Res. A. (Accel.)* 442, 216 (2000).
34. D. Morrison, *Electronic Design* **48**, 30 (2000).
35. M. M. Blouke, J. R. Janesick, and J. E. Hall, *Optical Eng.* **22**(5), 607 (1983).
36. M. D. Gregg and D. Minniti, *Publ. Astron. Soc. Pacific* **109**, 1062 (1997).
37. H. U. Keller and co-workers, *J. Phys. E (Sci. Instr.)* **20**(6), 807 (1987).
38. K. P. Klaasen, M. C. Clary, and J. R. Janesick, *SPIE J.* **331**, 376 (1982).
39. K. P. Klassen and co-workers, *Opt. Eng.* **38**, 1178 (1999).
40. C. D. Murray, *J. Br. Interplanetary Soc.*, **45**(9), 359 (1992).
41. J. V. Sweedler, K. L. Ratzlaff, and M. B. Denton, eds., *Charge-Transfer Devices in Spectroscopy*, VCH Publishers, New York, 1994.
42. C. Lengacher and co-workers, *Am. J. Phys.* **66**, 1025 (1998).
43. T. W. Barnard and co-workers, *Anal. Chem.* **65**, 1231 (1993).
44. D. M. Rowley, M. H. Harwood, R. A. Freshwater, and R. L. Jones, *J. Phys. Chem.* **100**, 3020 (1996).
45. J. C. Sutherland and co-workers, *J. Anal. Biochem.* **163**, 446 (1987).
46. E. Borroto and co-workers, *Gastr. Endoscopy* **50**, 684 (1999).
47. Z. Szigeti, P. Richter, and H. K. Lichtenhaler, *J. Plant Phys.* **148**, 574 (1996).

48. P. M. Epperson, R. D. Jalkain, and M. B. Denton, *Anal. Chem.* **61**, 282 (1989).
49. G. A. T. Duller, L. BotterJensen, and B. G. Markey, *Radiat. Meas.* **27**, 91 (1997).
50. T. W. Barnard, M. I. Crockett, J. C. Ivaldi, S. L. Lundberg, and E. F. Young, *1992 Pittsburgh Conference*, New Orleans, paper no. 990.
51. T. W. Barnard, M. I. Crockett, J. C. Ivaldi, S. L. Lundberg, and E. M. Ziegler, *1992 Pittsburgh Conference*, New Orleans, paper no. 991.
52. I. B. Brenner, S. Vats, and A. T. Zander, *J. Anal. Atom. Spectrose.* **14**, 1231 (1999).
53. R. L. McCreery, in Ref. 37, pp. 227–279.
54. A. Wang, L. A. Haskin, and E. Cortez, *Appl. Spectrose.* **52**(4), 477 (1998).
55. A. Wang, B. L. Jollif, and L. A. Haskin, *J Geophys. Res.* **104**(E11), 27,067 (1999).
56. J. Hynecek, *IEEE Trans. Electron Dev.* **ED-38**(5), 1011 (1991).
57. J. A. Gregory, B. E. Burke, B. B. Kosicki, and R. K. Reich, *Nucl. Instrum.Methods. Phys. Res., Sect. A.* **436**, 1 (1999).
58. P. E. Pool, R. Holtom, D. J. Burt, and A. D. Holland, *Nucl. Instrum.Methods. Phys. Res., Sect. A.* **436**, 9 (1999).
59. S. Tsuneta and co-workers, *Solar Phys.* **136**(1), 37 (1991).
60. D. N. Burrows and co-workers, in O. H. W. Siegmund, ed., *EUV, X-Ray, and Gamma-Ray Instrumentation for Astronomy III, Proc. SPIE* **1743**, 72 (1992).
61. R. D. Thom, T. L. Koch, J. D. Langan, and W. J. Parrish, *IEEE Trans. Electron Devices* **ED-27**(1), 160 (1980).
62. M. A. Kinch, R. A. Chapman, A. Simmons, D. D. Buss, and S. R. Borrello, *Infrared Phys.* **20**, 1 (1980).
63. D. K. Schroder, *Appl. Phys. Lett.* **25**(12), 747 (1974).
64. K. Y. Han, R. Iyer, M. Hafich, G. Y. Robinson, and D. L. Lile, *Electron. Lett.* **28** (19), 1795 (1992).
65. M. Wadsworth and co-workers, *IEEE Trans. Electron Dev.* **ED 42**(2), 244 (1995).
66. W. Runyon, in M. Grayson, ed., *Encyclopedia of Semiconductor Technology*, John Wiley & Sons, Inc., New York, 1984, p. 809.
67. D. J. Burt, “Fabrication Technology for Charge-Coupled Devices”, in M. J. Howes and D. V. Morgan, eds., *Charge Coupled Devices and Systems*, John Wiley & Sons, Inc., New York, 1979.
68. J. Hynecek, *IEEE Trans. Electron Dev.* **ED-28**(5), 483 (1981).
69. J. R. Janesick and co-workers, in M. M. Blouke and D. Pophal, eds., *Optical Sensors and Electronic Photography, Proc. SPIE* **1071**, 153 (1989).
70. R. H. Bube, *Solar Cells*, in Ref. 15.
71. R. H. Bube, *Photoconductivity of Solids*, John Wiley & Sons, Inc., New York, 1960.
72. A. Campion, J. Brown, and W. H. Grizzle, *Surf. Sci.* **115**, L153 (1982).
73. I. Fujieda and co-workers, *Opt. Eng.* **38**(12) 2093 (1999).
74. S. M. Sze, *Physics of Semiconductor Devices*, 2nd ed., John Wiley & Sons, Inc., New York, 1981.
75. M. Schanz and co-workers, *IEEE. Trans. Electron Dev.* **ED-44**(10), 1699 (1997).
76. N. Bluzer and A. S. Jensen, *Opt. Eng.* **26**(3), 241 (1987).
77. G. C. Bailey, *Proc. SPIE* **311**, 32 (1981).
78. B. H. Olson and co-workers, *Proc. IEEE CCD Workshop* (1997).
79. A. J. Blanksby and M. J. Loinaz, *IEEE Trans. Electron Dev.* **ED 47**(1), 55 (2000).
80. A. B. Dreeben and R. H. Bube, *J. Electrochem. Soc.* **110**, 456 (1963).
81. J. A. Beun, R. Nitsche, and H. U. Bolsterli, *Physica* **28**, 194 (1962).
82. “Metalorganic Vapor Phase Epitaxy 1992”, in the *Proceedings of the Sixth International Conference on Metalorganic Vapor Phase Epitaxy*, Cambridge, Mass., June 1992; 8–11, G. B. Stringfellow and J. J. Coleman, eds., *J. Crystal Growth*, **124**(1–4) (Nov. 1992).
83. V. V. Doushkina and co-workers, *Appl. Opt.* **35** 6115 (1996).
84. B. Matveev and co-workers, *Sensor. Actuat. B-Chem.* **51** 233 (1998).
85. A. Krier and Y. Mao, *Infrared Phys. Tech.* **38**(7) 397 (1997).
86. E. H. Putley, “Lead Sulphide, Selenide and Telluride”, in C. A. Hogarth, ed., *Materials Used in Semiconductor Devices*, Wiley-Interscience, New York, 1965.
87. A. Carbone and P. Mazzetti, *Phys. Rev. B-Cond. Matt.* **57**(4) 2454 (1998).
88. G. Giroux, *Can. J. Phys.* **41**, 1840 (1963).
89. W. F. Kosonocky, *Proc. SPIE* **1308**, 2 (1990).
90. B. Capone and co-workers, *Opt. Eng.* **18**(5), 535–541 (1979).

91. M. Kimata, M. Dneda, N. Yutani, S. Iwadi, and N. Tsubouchi, *IEEE Solid State Circuits*, **SC 22**(6), 1124–1129 (1987).
92. C. A. Gresham, D. A. Gilmore, and M. B. Denton, *Appl. Spectrose.* **53**(10) 1177 (1999).
93. C. Hilsum and A. C. Rose-Innes, *Semiconducting III–V Compounds*, Pergamon Press, New York, 1961.
94. J. T. Wimmers, R. M. Davis, C. A. Niblack, and D. S. Smith, *Proc. SPIE*, **930**, 125–138 (1988).
95. S. R. Jost, V. F. Meikleham, and T. H. Myers, in R. F. C. Farrow, J. F. Schetzina, and J. T. Cheung, eds., *Symposia Proceedings of the Material Research Society*, Pittsburgh, Pa., 1987, p. 429.
96. P. Mohan and co-workers, *J.Crystal Growth* **200**(1–2) 96 (1999).
97. A. Phillips and co-workers, *Astrophys. J.* **527**(2) 1009 (1999).
98. C. A. Castro and J. H. Tregilgas, *J. Crystal Growth* **86**, 138–145 (1988).
99. T. Tang, M. H. Kalisher, A. P. Stevens, and P. E. Herning, in Ref. 70, p. 321.
100. G. N. Pultz and co-workers, *J. Vacuum Sci. Technol. B* **9**(3), 1724–1730 (1991).
101. M. A. Kinch, S. R. Borrello, and A. Simmons, *Infrared Phys.* **17**, 127 (1977).
102. M. Itoh, H. Takigawa, and R. Ueda, *IEEE ED* **27**(1), 150–154 (1980).
103. C. T. Elliott, “Infrared Detectors”, in Ref. 15.
104. A. Józwikowska, K. Józwikowski, and A. Rolgalski, *Infrared Phys.* **31**(6), 543–554 (1991).
105. C. T. Elliott, D. Day, and D. J. Wilson, *Infrared Phys.* **22**, 31–42 (1982).
106. L. O. Bubulac, *J. Crystal Growth*, **86**, 723–734 (1988).
107. J. P. Rosebeck, R. E. Starr, S. L. Price, and K. J. Riley, *J. Appl. Phys.* **53**(9), 6430–6440 (1982).
108. R. B. Bailey and co-workers, *IEEE ED* **38**(5), 1104–1109 (1991).
109. J. P. Rode, *Infrared Phys.* **24**(5), 443–453 (1984).
110. R. E. DeWames and co-workers, *J. Crystal Growth*, **86**, 849–858 (1988).
111. Y. Nemirovsky, D. Rosenfeld, R. Adar, and A. Kornfeld, *J. Vac. Sci. Technol.* **7**(2), 528 (1989).
112. P. R. Norton, *Optical Eng.* **30**(11), 1649–1663 (1991).
113. P. R. Bratt, “Impurity Germanium and Silicon Infrared Detectors”, in R. K. Willardson and A. C. Beer, eds., *Semiconductors and Semimetals*, Vol. 12, Academic Press, Inc., New York, 1977.
114. R. D. Nelson, *Optical Eng.* **16**(3), 275–283 (1977).
115. D. H. Pommerrenig, *Proc. SPIE*, **443**, 144–150 (1984).
116. S. B. Stetson, D. B. Reynolds, M. G. Staplebroek, and R. L. Stermer, *Proc. SPIE*, **686**, 48–65 (1986).
117. J. Wolf, *Opt. Eng.* **33**(5), 1492 (1994).
118. S. D. Gunapala and co-workers, *IEEE Trans. Electron Dev.* **ED-44**(1), 45 (1997).
119. S. D. Gunapala, B. F. Levine, L. Pfeiffer, and K. West, *J. Appl. Phys.* **69**, 6517 (1991).
120. S. D. Gunapala and co-workers, *IEEE Trans. Electron Dev.* **ED-45**(1), 1890 (1998).
121. S. D. Gunapala and S. V. Bandara, “Quantum Well Infrared Photodetector (QWIP) Focal Plane Arrays”, in H. C. Liu and F. Capasso, eds., *Semiconductors and Semimetals*, Vol. 62, Academic Press, Inc., New York, 1999.
122. V. J. Realmuto, A. J. Sutton, and T. Elias, *J. Geo. Phys. Res.* **102**, 15057 (1997).
123. S. D. Gunapala and co-workers, *Proc. SPIE.* **3379**, 382 (1998).
124. U.S. Pat. 5,288,649 (Feb. 22, 1994), W. F. Keenan (to Texas Instruments Inc.).
125. R. A. Wood, “Monolithic Silicon Microbolometer Arrays”, in R. K. Willardson and E. R. Weber, eds., *Semiconductors and Semimetals*, Vol. 47, Academic Press, Inc. New York, 1997.

MARK WADSWORTH
Jet Propulsion Laboratory